CLOUD IMPACT PARAMETERS DERIVED FROM A-TRAIN SATELLITE, ERA-INTERIM, MERRA-2 AND THEIR RELATIONSHIP TO THE ENVIRONMENT

A Thesis

by

LU SUN

Submitted to the Office of Graduate and Professional Studies of
Texas A&M University
in partial fulfillment of the requirements for the degree of

MASTER OF SCIENCE

Chair of Committee,	Anita D. Rapp
Committee Members,	Courtney Schumacher
	Huilin Gao
	Yangyang Xu
Head of Department,	Ramalingam Saravanan

May 2019

Major Subject: Atmospheric Sciences

ABSTRACT

Cloud feedback remains one of the largest sources of uncertainty in model climate sensitivity estimates, partly because of the complicated interactions between convective processes, radiative effects, and the large-scale circulation. Cloud radiative effects and precipitation processes have been linked in both deep convective clouds (DC) and low cloud regimes, which points to the importance of understanding the connections between the latent heating from precipitation and surface and atmospheric cloud radiative effects. In this paper, cloud impact parameters (CIPs), including G_c, A_c and N_c and energy and water coupling parameters (EWCPs) are examined. The two EWCPs, the surface radiative cooling efficiency, R_c and the atmospheric heating efficiency, R_h are used to characterize how efficiently a cloud can heat the atmosphere or cool the surface per unit rain. EWCPs link both cloud radiative properties and precipitation properties together to demonstrate the synergistic effects of the cloud-precipitation-radiation interaction (CPRI). Global distributions of CIPs and EWCPs are highly dependent on cloud regimes and reanalyses fail to simulate strong R_c and R_h over deep convection regions in the Indo-Pacific warm pool region, but produce stronger R_c and R_h over marine stratocumulus regions. Together, these indicate the possibility that the variability of the Walker circulation simulated by reanalysis is underestimated. To understand how the environment modulates the EWCPs, the EWCPs from A-Train observations, ERA-Interim and MERRA-2 datasets are conditionally sampled by dynamic and thermodynamic variables including vertical pressure velocity (ω), sea surface temperature (SST), and column water vapor (CWV). The dynamic regime controls the sign of R_h, while the CWV appears to be the larger control on the magnitude. The magnitude of R_c is highly coupled to the dynamic regime. Observations also show two thermodynamic regions of strong R_c, at low SST and

CWV and at high SST and CWV, only the former of which is captured by the reanalyses. The results in this paper can be a reference for improving parameterizations important for coupling the energy and water cycles in global climate models.

ACKNOWLEDGEMENTS

First, I would like to express my gratitude and respect to my advisor, Dr. Anita Rapp, who gave me the chance to study in both the United States and Texas A&M University. I learned much expertise on satellite meteorology, multiple new research ideas and decent English language in scientific papers under Dr. Rapp's guidance. These will benefit me a lot in my long-term career. I am also grateful to my other thesis committee members, Dr. Courtney Schumacher, Dr. Yangyang Xu and Dr. Huilin Gao for their time to evaluate my research work. Without their comments and feedbacks, I cannot wrap up my research work and thesis. Their encouragement as well as criticism have shaped me to become a better researcher.

I would also like to thank my friends and colleagues. I would never forget the time we spent together and their company. They are always patient and kind to listen to me when I need help, no matter on academic discussion or trivial matters in life. Special thanks give to my office and group mate Kyle Wodzicki and Kevin Smalley who help a lot during my study here.

Last but not least, I feel greatly indebted to my dear parents and family for their persistent patience, continuous support and encouragement during these years. Thank you and I love you forever.

CONTRIBUTORS AND FUNDING SOURCES

Contributors

This work was supervised by a thesis committee consisting of Professor Anita Rapp of the Department of Atmospheric Sciences.

All other work conducted for the thesis was completed by the student independently.

Funding Sources

This research was sponsored by NASA energy and water cycle study (NEWS) Grant NNX15AD13G

NOMENCLATURE

AMSR-E	Advanced Microwave Scanning Radiometer for EOS
A-Train	The After Train
CALIPSO	Cloud-Aerosol Lidar and Infrared Pathfinder Satellite Observations
CIP	Cloud Impact Parameters
CPR	Cloud Profiling Radar
CPRI	Cloud-Precipitation-Radiation Interaction
CRF	Cloud Radiative Forcing
CWV	Column Water Vapor
DC	Deep convective Clouds
ECMWF	European Centre for Medium-Range Weather Forecasts
ENSO	El Niño Southern Oscillation
EOS	Earth Observing System
ERA-Interim	ECMWF Reanalysis Interim
EWCPs	Energy and Water cycle Coupling Parameters
GCM	General Circulation Model
GPROF	Goddard Profiling Algorithm
ITCZ	The Inter Tropical Convergence Zone
MCSs	Mesoscale Convective Systems
MERRA-2	The Modern-Era Retrospective Analysis for Research and Applications, V2
MJO	Madden-Julian Oscillation
MODIS	Moderate Resolution Imaging Spectroradiometer
JPL	Jet Propulsion Laboratory

NASA	National Aeronautics and Space Administration
NWP	Numerical Weather Prediction
PRs	Precipitation Rates
SST	Sea Surface Temperature
TOGA COARE	Tropical Ocean Global Atmosphere Coupled Ocean-Atmosphere Response Experiment

TABLE OF CONTENTS

LIST OF FIGURES

1. INTRODUCTION

Our climate is determined by the flows of energy into and out of the planet and to and from Earth's surface. But regional differences in the character of clouds and precipitation play significant roles in defining the gradients of atmospheric heating that drive atmospheric circulations. The response of the character of clouds and precipitation to changes in their environment, therefore, plays a significant role in determining the impacts of global climate change. Figure1.1 is a general energy and hydrological cycle schematic diagram from Stephens et al. (2012). This figure illustrates the importance of clouds in the top of atmosphere and surface radiation budgets. In the shortwave, clouds can impede the incoming solar radiation and cool the surface. In the longwave, clouds can also trap the outgoing longwave radiation from the surface and act as a greenhouse to make the atmosphere warmer. Overall, clouds work to reorganize the distribution of the surface and atmospheric energy budgets, which clearly impacts the necessary net latent heat flux, and thus precipitation, to maintain energy balance. This redistribution of precipitation and latent heating will feedback on cloud formation and the energy budget through its link to the large-scale circulation and the environment, so the interactions act as a coupled system. However, cloud-precipitation-radiation interactions are so complex that effort in studying the relationship between precipitation and radiation in different clouds and environmental regimes is still needed. The role of clouds in climate forcing, which highly depends on cloud macro- and micro- physical properties, remains one of the largest uncertainties in current climate projection (Bony and Dufresne 2005; Randall et al. 2007; Dessler, 2010; Choi et al. 2014 Bony et al. 2015; Ceppi et al. 2017). The macro- and microphysical properties impact both cloud radiative effects and precipitation intensity (Mace et al. 2017; Wood et al. 2012). To accurately predict cloud

feedbacks in the climate system, two elements should be further understood: the ability of climate models and physical parameterizations to produce cloud and precipitation from changing atmospheric states and the ability to use these cloud properties to estimate the radiative energy fluxes that, in turn, heat or cool the surface (Xu et al. 2005; 2016).

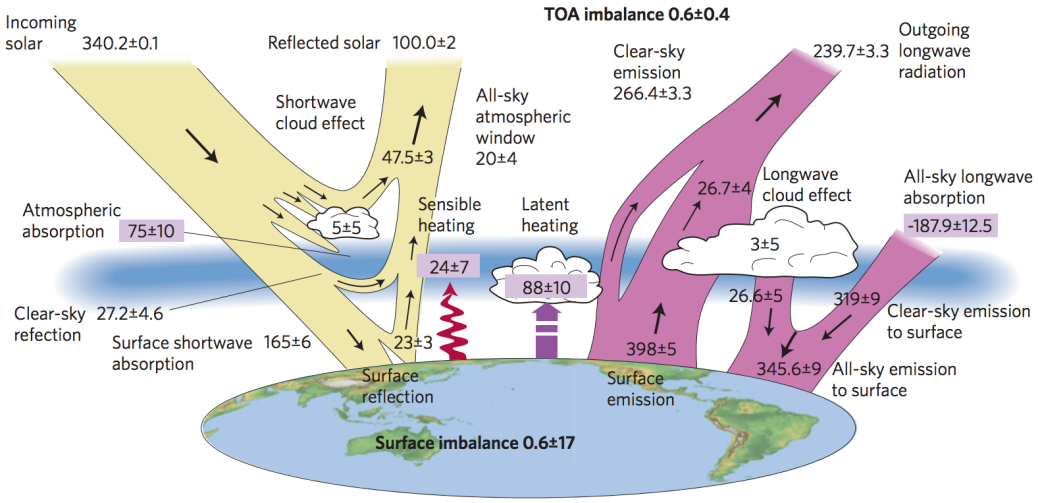

Figure 1.1: The global annual mean energy budget of Earth for the approximate period 2000-2010. All fluxes are in W/m^2, with solar fluxes in yellow and infrared fluxes in pink. The four flux quantities in purple-shaded boxes represent the principal components of the atmospheric energy balance. Source: Stephens et al. (2012).

As previously mentioned, cloud radiative effects and cloud feedback are highly connected to the precipitation process and the efficiencies in converting cloud condensate to surface precipitation (Stevens and Bony 2013; Bony et al. 2015). These links between the water and energy

cycles occur across a variety of spatial and temporal scales. At global annual mean timescales energy constrains precipitation, with precipitation increases primarily constrained by atmospheric radiative cooling (Held and Soden 2006; Stephens and Ellis 2008; O'Gorman, P.A. et al. 2012; Pendergrass and Hartmann 2014; Dinh and Fueglistaler 2017). Because the cloud radiative influence on the exchange of radiative fluxes between the atmosphere and surface are intimately linked with the water cycle through radiative-convective balance, the strength and location of cloud radiative effects and precipitation intensity is not independent and their relative magnitudes in global models depend strongly on the way clouds and convection are parameterized. The coupling of radiation-precipitation occurs across scales ranging from those of climatic scale (Allan et al. 2009; Previdi et al. 2010; Andrew et al. 2010; O'Gorman, P.A. et al. 2012), El Niño and Southern Oscillation (ENSO) (L'Ecuyer et al. 2006), Madden-Julian Oscillation (MJO) (Kim et al. 2015) and mesoscale convective systems (MCSs) (Bouniol et al. 2016), which should be accurately represented for models to simulate atmospheric radiative heating and cooling successfully. Failing to simulate the coupling of radiation-precipitation relationships at each spatial and temporal scale will bring large uncertainties in representing cloud cover, precipitation (both stratiform precipitation and convective precipitation) and thermodynamic forcing (Wilcox et al. 2001; O'Brien et al. 2013; Betts et al. 2014; Calisto et al. 2014). The phase of ENSO and MJO and the coupling with large-scale global circulation may also be misrepresented and lead to large biases in climate models and reanalysis if the radiation-precipitation coupling relationship is not well represented.

The way that clouds and precipitation are currently parameterized and coupled in Global Circulation Models (GCMs) is known to produce errors in radiative and latent heating distributions, such as insufficient low cloud cover in subtropical subsidence regions (Kay et al. 2012), warm sea

surface temperature (SST) biases in the southeast Pacific (Yu and Mechoso 1999; Dai et al. 2003; Li et al. 2004), the presence of a ubiquitous tropical rain band south of the equator (Waliser et al. 2003; Masunaga and L'Ecuyer 2011), premature onset of deep convection particularly over land (Dai and Trenberth 2004; Grabowski et al. 2006; Clark et al. 2007), the lack of Madden-Julian Oscillation (MJO) (Lee et al. 2001), and underestimates of the Walker circulation response to El Nino (L'Ecuyer and Stephens, 2007; Kociuba and Power 2015). The role of the coupled cloud–radiation interaction also affects the simulation of the MJO (Kim et al. 2013) and can amplify the warm El Nino phases of the El Nino-Southern Oscillation (ENSO) (Radel et al. 2016).

In addition to cloud-precipitation-radiation biases in climate models, there are also biases between reanalysis and observations, even though reanalysis is constrained by observations. Reanalysis-modeled clouds, radiation, and precipitation generally agree with observations reasonably well at the global mean scale, however, large biases occur at the regional scale. Dolinar et al. (2016) compared five reanalysis precipitation rates (PRs) with those from the Tropical Rainfall Measurement Mission (TRMM) and found reanalysis PRs overestimate the large-scale TRMM mean by 3% - 20 %, and also overestimate PRs in both ascent and subsidence regimes. PR biases over the ascent regime are an order of magnitude larger than those over the descent regime. Also, a lack of mid-level and/or low clouds, CWV, anomalous temperature structures and overestimated atmospheric stability represented by stronger subsidence in reanalysis results in radiative and precipitation biases at the same time (Naud et al. 2004; Griggs et al. 2008; Liu et al. 2016; Stengel et al. 2018). Both reanalysis and some climate models may have cloud, convection, or boundary layer scheme problems that lead to a large bias in individual weather systems and an inability to simulate the correct surface solar radiation (Naud et al. 2014), as well as global precipitation (Bodas-Salcedo et al. 2007). Approximations used in the model's representation of

moist processes strongly affect the quality and consistency of both cloud radiative forcing (CRF) and the hydrological cycle (Dee et al. 2011; Bosilovich et al. 2017).

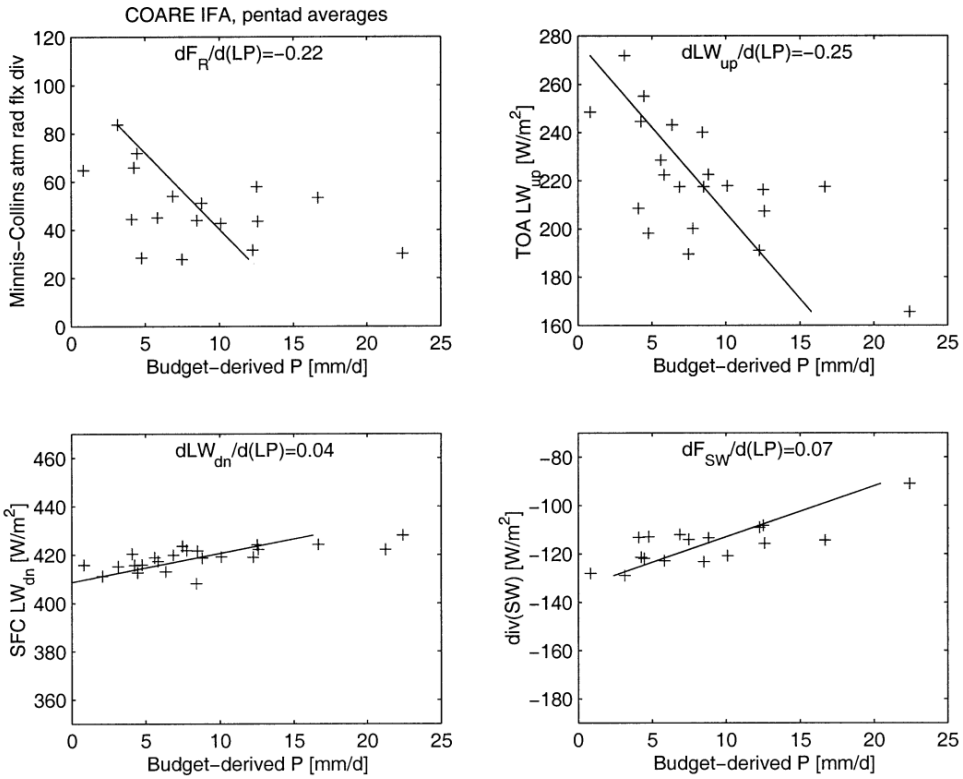

Figure 1.2: Scatterplots of net atmospheric radiative heating, TOA and surface longwave radiative fluxes, and tropospheric shortwave absorption vs IFA-mean precipitation P for all pentads in which data are available during TOGA COARE (1 NOV 1992-28 Feb 1993). In each plot, the line is a least squares fit of P on the other plotted variable, and the line slope is given in the top center of each panel. Source: Bretherton et al. (2002).

Because of the link between precipitation and atmospheric radiative fluxes, some numerical models - such as the minimal model of a moist equatorial atmosphere of Fuchs and Raymond

(2001) and the coupled ocean-atmosphere model of Bretherton and Sobel (2002) and Sobel and Gildor (2003) - assume a linear relationship is assumed to parameterize radiative heating and cooling processes. In these models, they fixed the relationship between CRF and precipitation, assuming that clouds reduce the clear-sky radiative cooling and surface cooling by an amount proportional to precipitation. Their fixed cloud-radiation feedback parameter was set equal to 0.2 based on five-day averaged surface and satellite radiation and precipitation measurements from Tropical Ocean Global Atmosphere Coupled Ocean-Atmosphere Response Experiment (TOGA COARE) as shown in Figure 1.2. They note that the uncertainties are as large as 50%. In a study of the effects of SST hot spots, Sobel and Gildor (2003) tested the sensitivity of their model to variations in their cloud-radiation feedback parameter. Figure 1.3a shows their sensitivity test for variations in this parameter with values between 0.2 and 0.3 showing a bifurcation, which means that the model behavior changes from a stable steady state to nonlinear oscillations at some point. The results clearly show a link between SST and the cloud-radiation feedback parameter. Figure1.3b shows that the period of the oscillation increases slightly from 70 to 82 days as the feedback parameter increases. Overall, this implies a relationship between the cloud-radiation feedback parameter, SST, and the time scales of variation and that this parameter is unlikely to be constant. These studies imply further investigation is needed to evaluate the true range of this parameter, which is vital for future model developments and improvements.

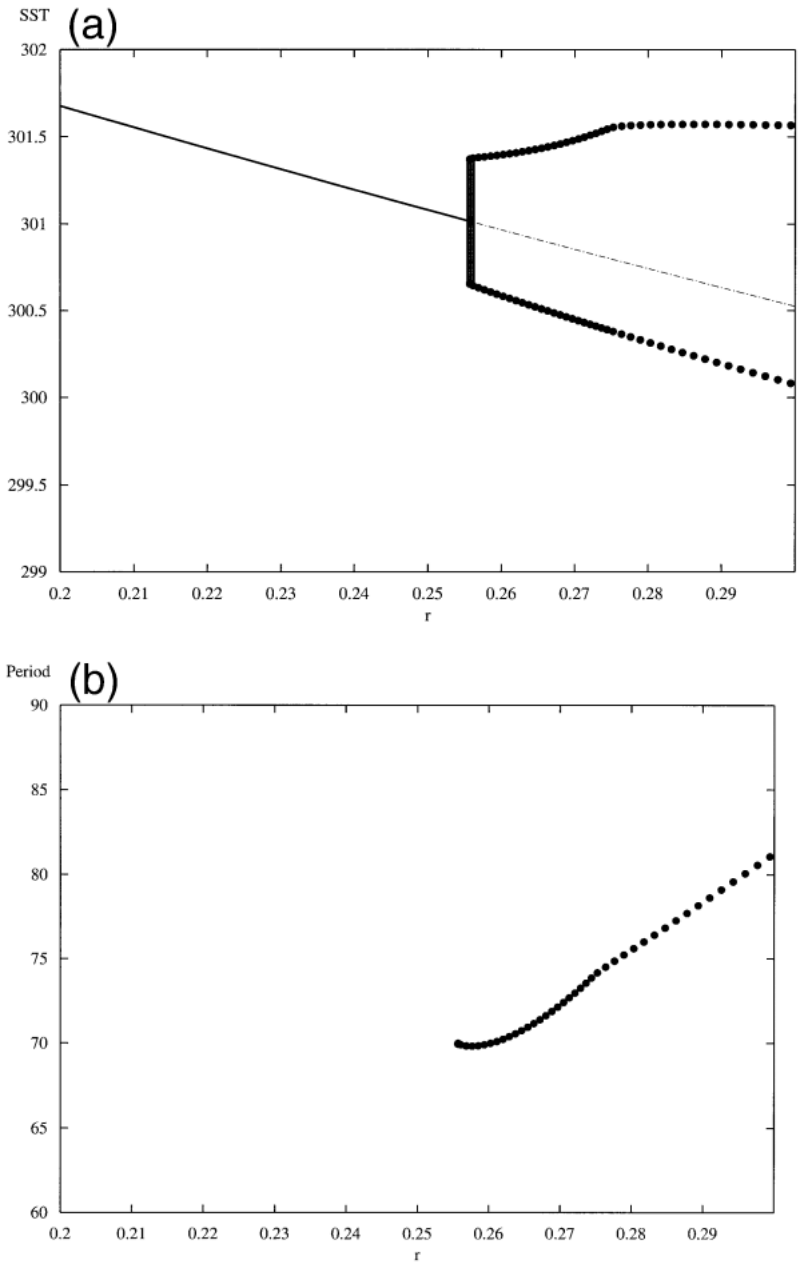

Figure 1.3: (a) Variation in SST and (b) the period of the oscillation as r is varied. Solid line represents a stable steady state. The solid circles indicate the max and min values of the stable limit cycle in (a) and the period in (b). Source: Sobel and Gildor (2003).

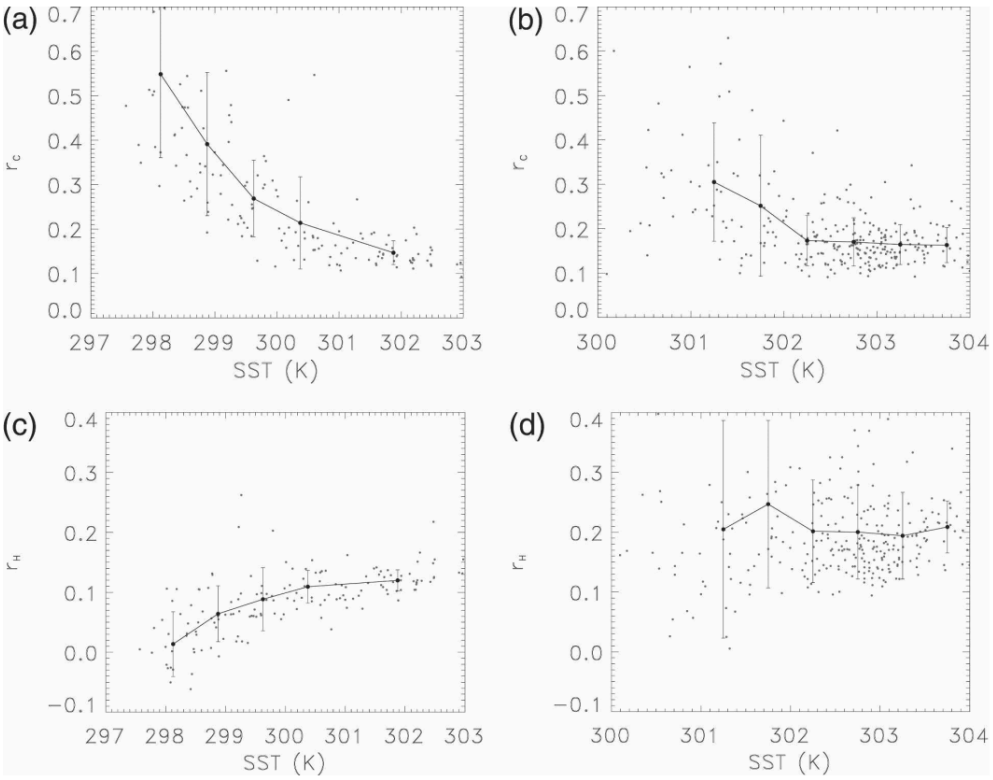

Figure 1.4: SST vs r_c. (a) in the Tropical Eastern Pacific (TEP) and (b) in the Tropical Western Pacific (TWP). (c), (d) Equivalent results for SST vs r_H for each region. Each data point represents a 20-day average at a resolution of 10°×10°. The solid lines and error bars represent the mean and standard deviation of each parameter in the indicated SST bin. Source: L'Ecuyer et al. (2006).

Emerging state-of-the-art satellite observations offer the opportunity to examine the radiation-precipitation relationship in more detail. In this context, L'Ecuyer et al. (2006) and Daloz et al. (2018) used TRMM and A-Train satellite observations to explore five monthly mean cloud radiative impact parameters (CIPs), including two energy and water cycle coupling parameters (EWCPs) that can connect the precipitation and cloud radiative effects to represent the cloud processes in climate models better: the greenhouse effect parameter, G_c, cloud albedo effect parameter, A_c, the ratio of cloud shortwave forcing (CSWF) to the corresponding cloud longwave

forcing (CLWF) at the top of the atmosphere, N_c, the surface cooling efficiency, R_c, and atmospheric heating efficiency, R_h. The surface cooling efficiency, R_c and atmospheric heating efficiency, R_h, represent how efficiently a precipitating cloud can cool the surface or heat the atmosphere per unit latent heat release from rainfall, respectively. These observational radiative efficiencies were first used to show the evidence of cloud feedback pathways associated with ENSO in the Pacific (L'Ecuyer et al, 2006) as illustrated in Figure 1.4. This figure demonstrates that clouds in the East Pacific heat the atmosphere more efficiently, and cool the surface less efficiently per unit rainfall with increasing SST, suggesting that changes in cloud characteristics may reinforce changes in the Walker circulation during El Niño events. Their estimates of R_c range from -0.7 to 0 and -0.1 to 0.4 for R_h at the monthly scale, as shown in Figure 1.4, which is a considerably larger range than the constant of 0.2 or the range from 0.2 – 0.3 used in the aforementioned modeling studies, suggesting biases may be more than 100%. In Daloz et al. (2018), they used A-Train observations and reanalyses to demonstrate and compare the global distribution and climatology of CIPs and EWCPs. While they examined the relationship between CIPs and EWCPs and vertical pressure velocity at 500hpa (ω_{500}), there was little discussion on the relationship to the thermodynamic environments. They also only examined the climatological mean CIPs, but the prior studies suggest considerable differences in these values at varying spatial and temporal scales. As the cloud radiative feedback on atmospheric circulation is still one of the most important topics in climate studies, the environmental impacts on CIPs and EWCPs should be studied in more detail to help improve the performance of GCMs and reanalysis (Bretherton et al. 2002, Bretherton et al. 2005; Muller et al. 2012; Bony et al. 2015). Also, the high sensitivity of the strength of the cloud-radiation feedbacks in the current models indicate that a specific

investigation of the coupling between radiative fluxes and precipitation in observations can provide a reference for model designers (Ying et al. 2016).

One of the key obstacles to accurately characterizing the feedback processes of clouds in climate is their dependence on the environments in which the clouds reside (Stephens 2005). Studies show that different cloud regimes, which determine the sign and strength of EWCPs, are associated with both dynamical and thermodynamical environmental variables, such as SST (Xu et al. 2009, Eitzen et al. 2010), column water vapor (CWV) and ω_{500}. Correspondingly, they also influence the coupling between precipitation and radiation (Wang et al. 2011). Kubar et al. (2012) reported a strong correlation between low topped cloud fractions and environmental variables, SST and ω_{500}. They also find that the correlation increases with increasing averaging time scale, from 1 day to about 15 days. Their findings indicate that when environmental variables change, such as SST and ω anomalies during an ENSO event, the fraction of clouds should change, leading to a corresponding change of CRF. These changes may strengthen or dampen large-scale circulation and impact precipitation intensity, suggesting additional studies on the variations in the coupling between CRF and precipitation with their environment should be conducted. The coupling of CRF and precipitation is needed in environmental control experiments (Larson et al. 1999) because both CRF and precipitation are influenced by SST and water vapor (Larson et al. 1999, 2003a, 2003b). However, in modeling experiments, they are often tested separately instead of coupled. Additionally, radiative heating/cooling and precipitation are constrained under radiative-convective equilibrium (RCE). Studies show that under RCE assumption, temperature and water vapor have positive feedback in atmospheric longwave cooling (Allan 2009; Allan 2011; Pendergrass and Hartmann 2014; Colman, 2015). But L'Ecuyer et al. (2006) demonstrated that RCE cannot be met locally due to the highly variable nature of the frequency, structure, and

radiative properties of clouds and precipitation, which also motivates further examination of the dependence of CIPs and EWCPs on the environment. In addition, studies of the environmental dependence of the coupling in CRF and precipitation may help to inform and constrain sub-grid cloud parameters represented in climate models.

Overall, the main goal of this study is to evaluate the range of CIPs and EWCPs in both A-Train satellite and reanalysis datasets and to understand how they are linked to the dynamic and thermodynamic environment. A comparison of the global distribution of A-Train-derived CIPs and EWCPs and reanalysis-derived CIPs and EWCPs at hourly timescales is first conducted. Then the observational and reanalysis EWCPs are conditionally sampled by environmental variables, SST, CWV and ω_{500}, to determine how well reanalyses capture interactions among radiation-precipitation coupling, thermodynamic environments, and the corresponding change of large circulation indicated by ω_{500}.

2. DATA AND METHODS

2.1 Satellite Observations

The near-simultaneous measurements from the CloudSat, CALIPSO, and Aqua satellites in the A-Train constellation, shown in Figure 2.1, provide the datasets used in this analysis. The CIPs and EWCPs are calculated from standard A-Train products from CloudSat-CALIPSO, including 2B-FLXHR-LIDAR (Stephens et al. 2002 and 2008; L'Ecuyer et al. 2008), 2B-GEOPROF-LIDAR (Stephens et al. 2002, 2008 and 2017; Sassen et al. 2008; Mace et al. 2009) and 2C-RAIN-PROFILE (Lebsock and L'Ecuyer 2011), and the Advanced Microwave Scanning Radiometer–Earth Observing System (AMSR-E) rainfall product, AE_RAIN (Wilheit 2003; Kummerow et al. 2010). CloudSat is a polar-orbiting satellite with a 98° orbital inclination carrying a 94 GHz (W-band) Cloud Profiling Radar (CPR), which is used to probe the vertical structure of clouds and precipitation (Stephens et al. 2008; Stephens et al. 2017; L'Ecuyer and Jiang 2010; Mace et al. 2014). CALIPSO uses the cloud-aerosol lidar with orthogonal polarization (CALIOP) to probe the vertical structure and properties of thin clouds and aerosols. With the combination of both CPR and CALIOP, there is an improved ability to detect thin cirrus and low clouds, especially when multiple layered clouds exist. The 2B-GEOPROF-LIDAR dataset provides the cloud layer and cloud top information to distinguish the heights and the number of cloud layers. The precipitation is provided by the 2C-RAIN-PROFILE dataset, which uses the two-way path integrated attenuation (PIA) of the entire atmospheric column to determine the presence of precipitation within the column (Haynes et al. 2007; Haynes et al. 2009; Stephens et al. 2008; Lebsock et al. 2011). However, the CPR has limitations in detecting heavy rain because of attenuation (Behrangi

et al. 2012). To mitigate this limitation, rain rate derived from AMSR-E observations is used whenever the AMSR-E rain rate exceeds 2C-RAIN-PROFILE. AMSR-E is a total power passive-microwave (MW) radiometer system on aboard NASA EOS Aqua satellite with twelve channels and six frequencies measuring brightness temperature at 6.925, 10.65, 18.7, 23.8, 36.5 and 89.0GHz. Rain rate and rain type over ocean are generated via Goddard Space Flight Center (GSFC) Profiling algorithm (GPROF) (Wilheit 2003). The AE_RAIN product uses the more up-to-date GPROF2010 (Kummerow et al. 2010; Kummerow et al. 2015). This study uses an existing rainfall subset that collocated AMSR-E rainfall products with the CloudSat track (Global Hydrology Resource Center/MSFC/NASA, 2009). One thing to note is that currently the CloudSat 2C-RAIN-PROFILE dataset is only applied over ocean (Lebsock et al 2011), so the EWCPs are only calculated over the ocean.

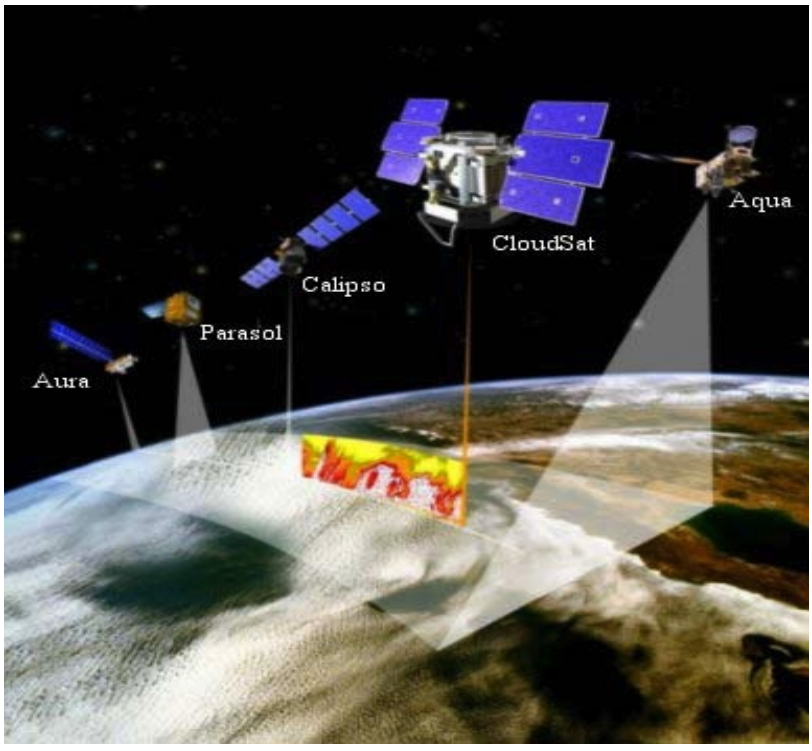

Figure 2.1: A-Train satellite constellation and their swaths and orbits

Radiative fluxes are used in the calculation of EWCPs and are provided by 2B-FLXHR-LIDAR (Stephens et al. 2008; L'Ecuyer et al. 2011), referred to hereafter as 2BFLX. 2BFLX blends information from the A-Train constellation including CloudSat's CPR, the CALIPSO satellite's CALIOP, and the Moderate Resolution Imaging Spectroradiometer (MODIS) and AMSR-E instruments on the Aqua satellite to generate vertically-resolved profiles of broadband radiation using a radiative transfer model (L'Ecuyer et al. 2008; Henderson et al. 2013). The underlying goal of the 2BFLX algorithm is to produce a vertically resolved radiative flux and heating rate dataset that is consistent with observed reflectivity from CloudSat's CPR. Vertical distributions of liquid and ice cloud effective radii and water contents from the level 2 cloud water content product are merged with ancillary temperature and humidity profiles from the European Centre for Medium-Range Weather Forecasts (ECMWF) analyses and surface albedo and emissivity data from the International Geosphere-Biosphere Programme (IGBP) global land surface classification to initialize broad-band radiative flux calculations via a two-stream, plane-parallel, doubling-adding radiative transfer model similar to that introduced by Ritter and Geleyn (1992). The specific model used in 2BFLX employs a Delta-Eddington formulation in six shortwave (SW) bands and a constant hemisphere formulation in twelve longwave (LW) bands. In general, Rayleigh scattering, gaseous absorption, and both absorption and scattering by condensed water (liquid and ice) are included. An explicit aerosol model compatible with the algorithm is also available and will be implemented once an ancillary aerosol data set for use with CloudSat has been generated, but has not been incorporated in this version of the algorithm.

The 2BFLX algorithm, with the combination of multisensor observations, brings a more accurate and comprehensive perspective in determining the radiative impacts of clouds and aerosols.

2.2 Reanalysis Data

This study compares the CIPs and EWCPs from two modern reanalyses, MERRA-2 and ERA-Interim with A-Train-derived products from September 2006 – December 2010 for 60°S - 60°N. The relationship between the environment and EWCPs is also evaluated.

2.2.1 MERRA-2

MERRA-2 (Gelaro et al. 2017; Bosilovich et al. 2015b; Bosilovich et al. 2016; Bosilovich et al. 2017) replaces the previous MERRA with increased resolution, improvements in the GEOS-5 model, and in the assimilation system. The new system enables assimilation of modern hyperspectral radiance and microwave observations as well as GPS-Radio Occultation datasets, and is the first long-term reanalysis that assimilates space-based observations of aerosol. After 2005 ozone observations are included. Several upgrades have been made to the physical parameterization schemes including an increase in reevaporation of frozen precipitation and cloud condensate (Molod et al. 2015). The new reanalysis dataset now contains a Tokioka-type trigger on deep convection as part of the relaxed Arakawa-Schubert convective parameterization (Moorthi and Suárez 1992; Cullather et al. 2014). In our studies, we use tavg1_2d_rad_Nx 1-hourly time-averaged data to calculate the radiative fluxes at surface and atmosphere and total precipitation from tav1_2d_flx_Nx 1-hourly time-averaged data to calculate the latent heating.

2.2.2 ERA-Interim

ERA-Interim (Dee et al. 2011) is a global atmospheric reanalysis beginning in 1979, developed by the European Center for Medium Range Forecasts (ECMWF). It is produced with a sequential data assimilation scheme, advancing forward in time using 12-hourly analysis cycles. In each cycle, available observations are combined with prior information from a forecast model to estimate the evolving state of the global atmosphere and its underlying surface. This involves computing a variational analysis of the basic upper-air atmospheric fields (temperature, wind, humidity, ozone, surface pressure), followed by separate analyses of near surface parameters (2m temperature and 2m humidity), soil moisture and soil temperature, snow and ocean waves. the analyses are then used to initialize a short-range model forecast, which provides the prior state estimates needed for the next analysis cycle.

ERA-Interim replaced the previous reanalysis dataset from the ECMWF, ERA-40. Between ERA-40 and ERA-Interim, changes to the convective and boundary layer cloud schemes were made. For example, the convective cloud scheme can now be triggered at night, which increases its atmospheric stability and therefore creates less precipitation (Dee et al. 2011). The new moist boundary layer scheme reduces the underestimate of stratocumulus clouds because of changes in the inversion strength and height (Kohler et al. 2011). Convection, vertical motion, radiative heating and turbulence are connected to cloud generation via the prognostic cloud scheme (Jakob 1998). The Rapid Radiative Transfer Model computes radiation (Mlawer et al. 1997). In our studies, we use the 3-hour surface flux variable and surface albedo to get the downward shortwave flux and the reflected upward shortwave flux. Radiative flux variables at TOA are obtained directly from ERA-Interim. Total precipitation from ERA-Interim is used to calculate the latent heating.

ERA-Interim also provides the environmental variables, SST, CWV, ω_{500}, which are used as the environmental variables that are matched with EWCPs.

2.3 Calculations of CIPs and EWCPs

The 2BFLX product is used to calculated the CIPs and EWCPs. G_c, the cloud greenhouse effect, and A_c, the cloud albedo effect, encapsulate the competing effects of clouds on the atmosphere. G_c is defined as the cloud impact on outgoing longwave radiation expressed as a fraction of surface emission. Following the clear-sky greenhouse parameter, G, introduced in Stephens and Greenwald (1991) we define:

$$G_c = -\frac{F^{\uparrow}_{LW,TOA,all} - F^{\uparrow}_{LW,TOA,clear}}{F^{\uparrow}_{LW,SFC}} \qquad (1)$$

where $F^{\uparrow}_{LW,TOA}$ and $F^{\uparrow}_{LW,SFC}$ represent the upwelling longwave (LW) fluxes at the top of the atmosphere (TOA) and surface (SFC) respectively. Cloud effects on shortwave radiation are characterized by their impact on albedo. A_c is defined as the difference in reflectivity resulting from clouds:

$$A_c = \frac{F^{\uparrow}_{SW,TOA,all} - F^{\uparrow}_{SW,TOA,clear}}{F^{\downarrow}_{SW,TOA}} \qquad (2)$$

A_c is closely related to cloud forcing, but includes a normalization by incoming solar radiation to partially remove the dependence on the time of day and latitude. Larger values of A_c indicate a higher albedo effect and therefore a cooling of the atmosphere through the clouds. A_c reflects the albedo effect of clouds, so we expect this parameter to be sensitive especially to bright clouds. N_c provides a dimensionless measure of the relative strengths of cloud albedo and greenhouse effects,

or the ratio of cloud shortwave forcing (CSWF) to the corresponding cloud longwave forcing (CLWF) at the TOA:

$$Nc = \frac{CSWF}{CLWF} = -\frac{\left(F^{\downarrow}_{SW,TOA} - F^{\uparrow}_{SW,TOA}\right)_{all} - \left(F^{\downarrow}_{SW,TOA} - F^{\uparrow}_{SW,TOA}\right)_{clear}}{F^{\uparrow}_{LW,TOA,all} - F^{\uparrow}_{LW,TOA,clear}} \quad (3)$$

where for low clouds $N_c > 1$, while $N_c < 1$ for thin high clouds. In other words, when N_c values are greater than (less than) 1, it indicates a net cooling (heating) at the top of the atmosphere.

The two EWCPs are calculated with the shortwave and longwave CRF from 2BFLX and the coincident CloudSat/AMSR-E precipitation. The radiative cooling efficiency, R_c, at the SFC is defined as:

$$Rc = \frac{F^{\downarrow}_{SW,SFC,all} - F^{\downarrow}_{SW,SFC,clear}}{LH} \quad (4)$$

where $F^{\downarrow}_{SW,SFC}$ is the downwelling SW flux that is evaluated in both clear-sky and all-sky conditions. Subscripts '*clear*' and '*all*' correspond to clear-sky and all-sky conditions respectively. R_c represents a cloud's ability to cool the surface per unit LH from rainfall, where LH is defined as the column latent heating from the precipitation reaching the surface and is calculated as

$$LH = \rho * q_v * RR \quad (5)$$

where ρ is the density of water, q_v is latent heat of vaporization for water, and RR is the average surface rainfall rate from CloudSat or AMSR-E. Similarly, the atmospheric radiative heating efficiency R_h describes a cloud's ability to heat the atmosphere per unit LH,

$$R_h = \frac{(\Delta F_{LW} - \Delta F_{SW})_{all} - (\Delta F_{LW} - \Delta F_{SW})_{clear}}{LH} \quad (6)$$

where $\Delta F_{LW} = F^{\uparrow}_{LW,SFC} - F^{\downarrow}_{LW,SFC} - F^{\uparrow}_{LW,TOA}$ and

$\Delta F_{SW} = F^{\downarrow}_{SW,TOA} - F^{\uparrow}_{Sw,SFC} - F^{\downarrow}_{SW,SFC} - F^{\uparrow}_{SW,TOA}$ are the LW and SW atmospheric radiative flux divergences, respectively, calculated between the SFC and TOA. The numerator of R_c is the

cloud forcing at surface, that is, the amount of incoming solar radiation that has been hindered by the clouds. The numerator of R_h is the total CRF of the atmosphere, while the denominator of both equations is latent heating that has been released by the precipitation from the clouds.

We use 2BFLX to calculate the fluxes during the daytime. The combination of 2C-RAIN-PROFILE and AMSR-E data provide the surface precipitation rate from which we can estimate latent heating as in Equation (4). Again, due to the known limitations of the 2C-RAIN-PROFILE dataset in heavy rain scenarios, AMSR-E-CloudSat collocated products are used when the CPR is judged as saturated based on a flag in the algorithm. Otherwise, the CPR rain rate will be used because CloudSat has the superior ability in detecting light and moderate rain (Behrangi et al. 2012; Lebsock et al. 2011).

Because the reanalysis precipitation is calculated based on the model moisture budget and must meet the budget equilibrium, sometimes the reanalysis precipitation has an extremely small value in one grid box. As Stephens et al. (2010) discussed, models produce precipitation approximately twice as often as that observed and make too much light rainfall. The reanalysis products analyzed here provided values as small as 10^{-12} mm/hr, which is well below any space borne precipitation sensor detection limits and also produces unrealistically large values of R_c and R_h. Here we use the minimum precipitation value of 6.4×10^{-5} mm/hr detected in the CloudSat dataset as a threshold to filter precipitation below this CloudSat minimum threshold. To compare the different reanalysis datasets to each other and to the observations, we download ERA-Interim and MERRA-2 dataset of 2.5° x 2.5° directly with inherent interpolation. Meanwhile, all the A-Train data are also averaged to a common 2.5° x 2.5° grid at 3-hourly temporal resolution. Each pixel from the A-Train datasets is matched to the nearest 3-hourly time step of the reanalysis datasets.

3. RESULTS

3.1 Global Distributions

An overview of the global distribution of the radiative CIPs from A-Train, ERA-Interim and MERRA-2 is presented in Figure 3.1. In the regions beyond 60°N or 60°S there is a lack of liquid surface precipitation (Stephen et al. 2008; L'Ecuyer et al. 2010; Lebsock and L'Ecuyer 2011; Mace et al. 2009; Mace et al. 2014), so these regions are removed because there are too few samples in each grid box to provide meaningful results for the EWCPs which is the main focus of this study.

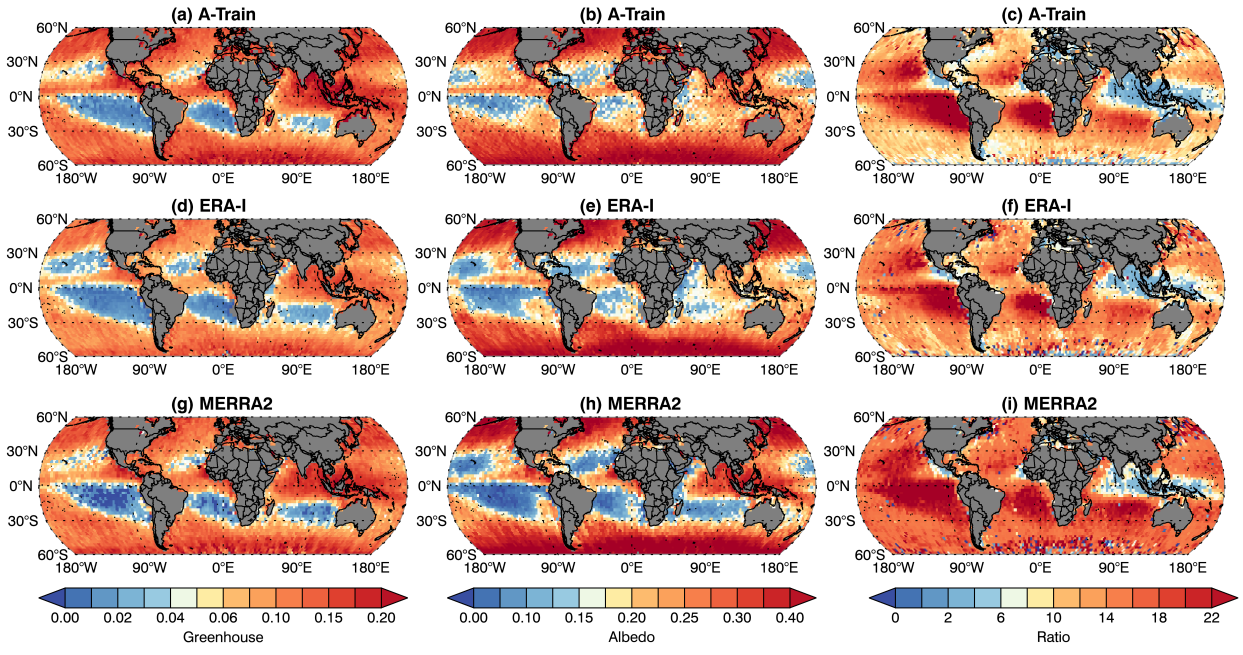

Figure 3.1: The global observed distributions of G_c (a, d, g) and A_c (b, e, h) and N_c (c, f, i) derived from A-Train (a-c), ERA-Interim (d-f) and MERRA-2 (g-i) from September 2006 - December 2010

From Figure 3.1 we can see that the patterns of G_c are highly correlated with the presence of high clouds which tend to appear over the tropics and at mid-latitudes. These regions tend to have a lot of convective clouds, which are known for their ability to trap longwave radiation. Over 45^{o}N and 45°S, the regions with high values of G_c are present over the Pacific and Atlantic Oceans for both hemispheres. However, these values are lower than over the tropics. At these latitudes, high values of G_c are due to the persistent presence of altostratus clouds. Because altostratus and convective clouds are high, and therefore cold, the energy they radiate to space is lower than it would be in clear-sky conditions, explaining their large greenhouse forcing. The top middle panel in Figure 3.1 shows the spatial map of A_c for the A-Train satellite observations. Contrary to G_c, high values of A_c mean a cooling of the atmosphere through the clouds. High values of A_c appear on the eastern side of the oceans where marine stratocumulus persist over the dark ocean background (Wood, 2012). Stratocumulus are low, optically thick clouds that reflect much of the incoming solar energy back to space, explaining their high values in A_c. On the other hand, because stratocumulus are low clouds, they have a similar temperature to the surface and radiate at nearly the same intensity as the surface explaining their weak greenhouse effect (cf. Figure. 3.1a).

The effect of clouds on the atmosphere is large around the equator and at midlatitudes for both the greenhouse and albedo effects, with different amplitudes. For albedo effects, it is likely due to the reflective alto- and nimbostratus in the midlatitude storm tracks and stratus dominant in the southern oceans. These low stratus clouds are also known for their high values in albedo due to their composition, which tend to be water drops or supercooled water. Large A_c values also

coincide with the band of deep convective clouds with high-altitude outflow in the ITCZ and along the Equator that reflects a lot of the solar energy back to space.

It is evident from Figure 3.1 that differences in the strength of the cloud albedo and greenhouse effects exhibit regional patterns that closely reflect the large-scale circulations. This signature is very clear in the right panels of Figure 3.1 that present the observed distributions of the dimensionless ratio of cloud SW to LW forcing, N_c. Deep convection over the tropics characterized by cold, bright clouds tops exhibits values of N_c near 1 (Kiehl 1994) because of the near-compensating effects between the shortwave reflection and the longwave heating. From Figure 3.1, we also see regions of N_c with values greater than 1 because of shallow clouds, which will increase the values of N_c over these regions. Therefore, the highest values of N_c appear in subsidence regions of the subtropics where bright marine stratocumulus clouds near the surface are dominant. High values of N_c in these regions mean that these clouds provide a net cooling of the atmosphere, while other types of clouds, such as tropical deep convective clouds, tend to have a neutral impact on the atmosphere.

Although the reanalyses tend to agree in the representation of the spatial patterns of all three CIPs, large significant differences in amplitude appear between the reanalyses and satellite observations. The average value of G_c in ERA-Interim is lower than A-Train and MERRA-2, although MERRA-2 shows lower G_c over marine stratocumulus regions. The other features are quite similar for all the A-Train and reanalyses. One of the obvious different features of A_c across the three is that MERRA-2 produces more widespread low A_c regions in subtropical latitudes of both hemispheres. It means that MERRA-2 tends to produce probably low shallow cloud fraction over these regions. However, it should be noted that Daloz et al. (2018) reported that A-Train may overestimate cloud albedo effect. For N_c, MERRA-2 shows higher values in most regions globally

compared to observations and ERA-Interim. It seems to contradict with the fact of underestimation of the shallow cloud fraction. However, from Figure3.1, there is not a prominent difference of G_c and A_c, which can be treated as a proxy for the numerator and denominator of N_c. We can infer that there are likely biases of MERRA-2 in simulating $F^{\uparrow}_{LW,SFC}$, which are apparently larger than the uncertainties in cloud cover. These uncertainties have been reported by Bosilovich et al. (2015b), Bosilovich et al. (2016) and Bosilovich et al. (2017). Several studies showed that reanalyses tend to have difficulty accurately representing cloud cover (Duynkerke and Teixeira, 2001, Steven et al. 2007, Uppala et al. 2005), which is often one of the main reasons for radiative biases.

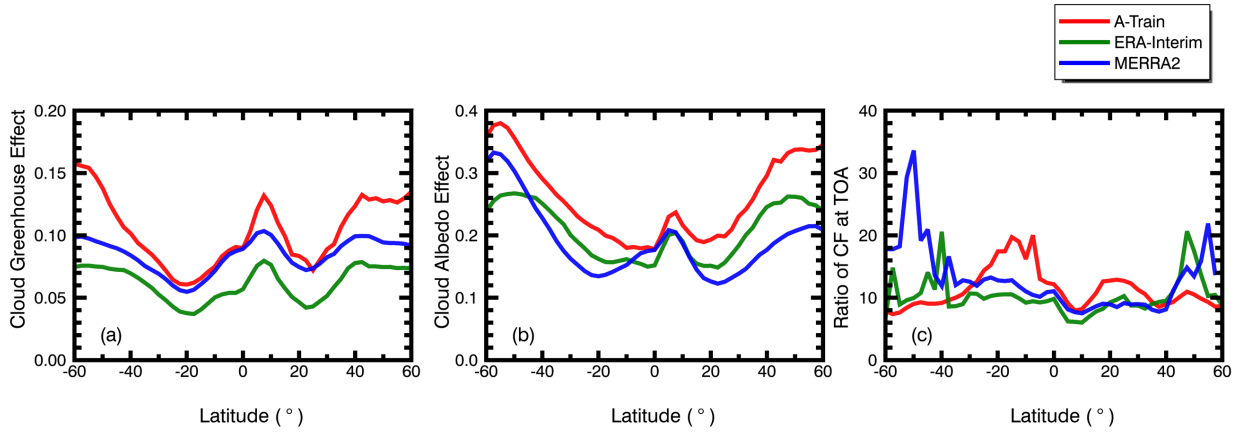

Figure 3.2: Zonal Mean of (a) G_c and (b) A_c and (c) N_c derived from A-Train, MERRA-2 and ERA-Interim from September 2006 - December 2010

Figure 3.2 summarizes the zonal mean of G_c, A_c and N_c for the observations and reanalyses. G_c and A_c have distinct equatorial and mid-latitude characteristics. At the equator, due to the cloud forcing induced by the deep convective clouds, there are both strong cloud greenhouse and cloud

albedo effects. Correspondingly, N_c at the equator is not large, consistent with the spatial distribution shown in Figure 3.1. Generally, the A-Train observations show relatively higher values than both ERA-Interim and MERRA-2, except for N_c, for which A-Train is higher in the subtropics, where the low cloud regimes contribute the most. ERA-Interim shows lower value for G_c globally, consistent with our previous discussion, while for MERRA-2, the higher values for N_c mainly come from midlatitudes.

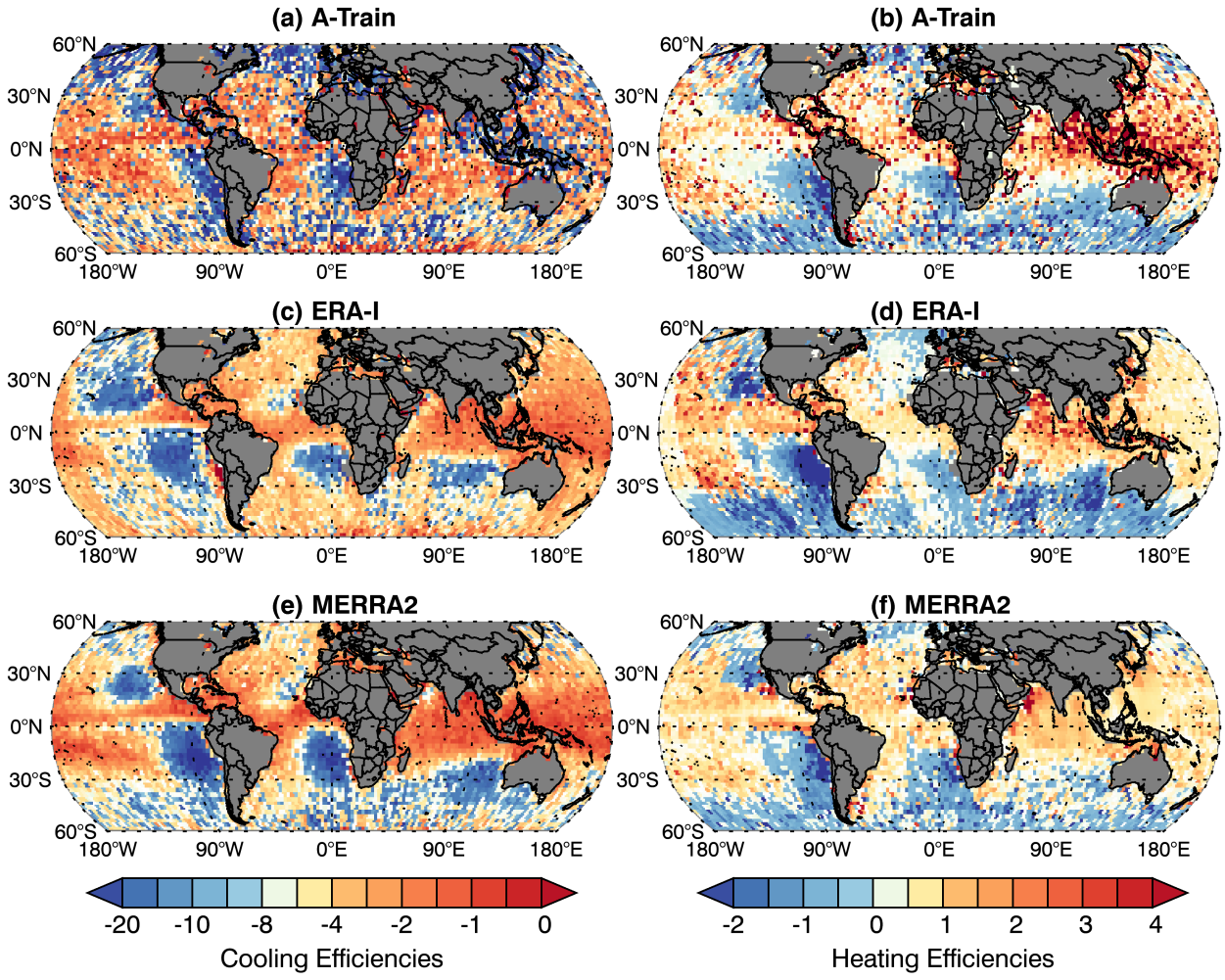

Figure 3.3: The global observed distributions of R_c (a, c, e) and R_h (b, d, e) derived from A-Train (a, b), ERA-Interim (c, d) and MERRA-2 (e, f) from September 2006 - December 2010

The global patterns of monthly-averaged R_c and R_h results have also been previously discussed in Daloz et al. (2018); however, at these long timescales it is possible that the radiation and precipitation may not actually be coupled. For example, it would be possible to capture the same monthly mean value of the EWCPs with the wrong distribution of clouds or with the wrong clouds producing precipitation. Because we are interested in the connection between precipitation and radiation on the timescales of the clouds and the timescales for which the parameterizations must operate in the reanalyses, the patterns of three hourly-averaged results are shown. They are similar to the patterns calculated from monthly mean fluxes, but with the main difference in magnitude, which is easily explained because precipitation varies more temporally and spatially than the radiative fluxes. As a result, when R_c and R_h are calculated at shorter time scales, the variation of R_c and R_h is larger than that of the monthly average timescale. From A-Train observations, there are clear patterns that correspond to the global distribution of predominant cloud regimes. Generally, marine stratocumulus regions in the south and north Pacific and south or west Atlantic (Wood et al. 2012; Hartmann et al. 1993), where clouds cool the surface and atmosphere most efficiently because precipitation is weak, correspond to the strongest negative R_c and R_h. Over the ITCZ and South Asia monsoon region, R_h is large and R_c is small. The Indo-Pacific warm pool region shows both strong R_c and R_h, which means that DC cools the surface and heats the atmosphere more efficiently per unit rainfall. In shallow cumulus regions (180°W~135°W, 10°S~25°S), both R_c and R_h are weaker than other regions.

Comparison with ERA-Interim and MERRA-2 in Figure 3.3 shows the global patterns are generally consistent, although some tropical regions show significant differences between A-Train and the reanalyses. One of these main biases appears over the Indo-Pacific warm pool. Reanalysis generally fail to simulate both large R_c and R_h there, although the reanalyses does generally capture

strong R_h over the South Asia (India) monsoon region, although not as strong as the A-Train estimates. One possible reason, at least for ERA-Interim, is that it underestimates the LW CRF at TOA over tropical regions due to biases in cloud fraction and the TOA radiative flux diurnal cycles (Itterly et al. 2014). Moreover, ERA-Interim overestimates precipitation in both ascending and descending regimes (Itterly et al 2014; Dolinar et al 2016). Figure 3.3d indicates that ERA-Interim R_h is generally more negative than other products over marine stratocumulus regions, which is likely caused by the SW biases reported by Dolinar et al. (2016). It has also been reported that there is stronger water cycle in MERRA-2 than the observations because modifications in the MERRA-2 model resulted in changes in ocean evaporation and atmospheric transport and excessive precipitation is generated in the Indo-Pacific warm pool (Bosilovich et al. 2015; Bosilovich et al. 2017; Gelaro et al. 2017). This may also explain why MERRA-2 R_h is slightly smaller than ERA-Interim over the South Asia (India) Monsoon region. Other differences appear over the eastern Pacific marine stratocumulus region, where reanalyses generally produce stronger R_c and negative R_h over a larger region, which means that the clouds cool the surface and atmospheric more efficiently per unit rainfall. While reanalyses are constrained by observations, such biases may have significant implications for freely running GCMs since the regional variations in R_c and R_h feedback on the large-scale circulation and could increase the potential lack of response to El Niño events. It also implies some limitations of models to represent the Walker and Hadley Circulations.

As previously mentioned, due to the sampling limitations of the sun synchronous A-Train satellites, R_c and R_h values were only compared with reanalysis for grid boxes when the satellites overpass it. Although not shown here, R_c and R_h were calculated from the full diurnal cycle available in the reanalyses. The climatological global patterns are still similar and still highly

depend on the distributions of the cloud regimes, however the regional differences with observations are amplified with weaker R_h and R_c in the warm pool and stronger R_h and R_c in subsidence regimes and the southern oceans.

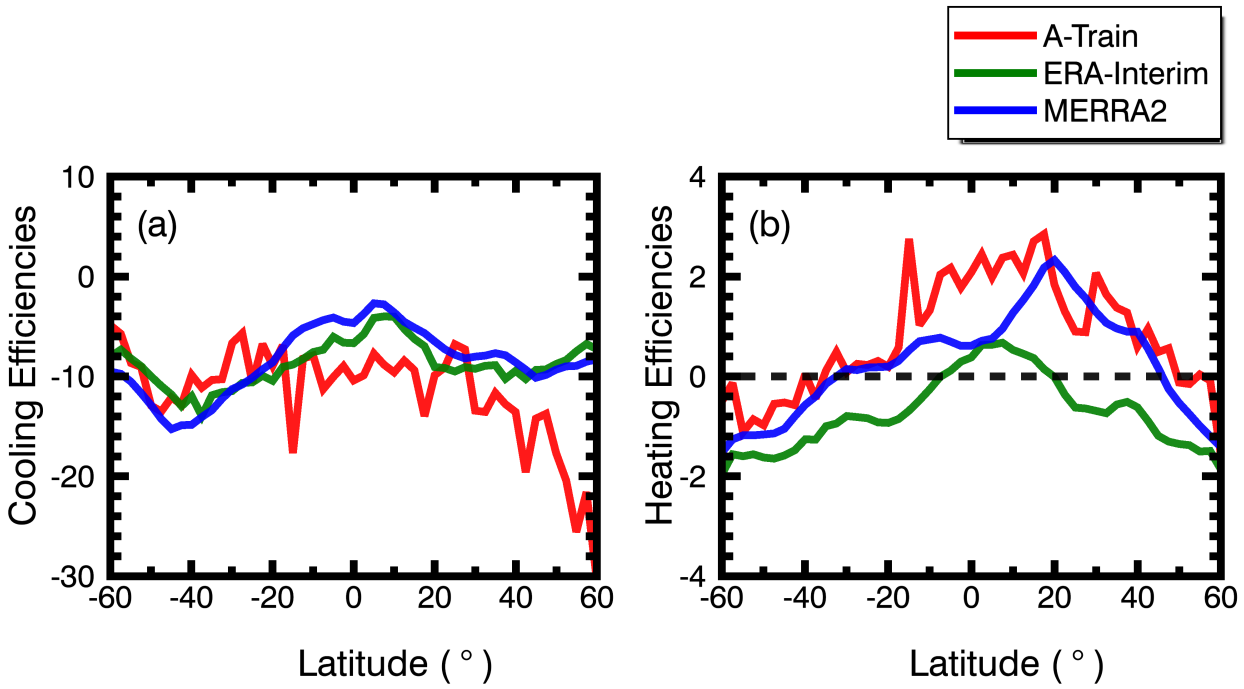

Figure 3.4: Zonal Mean of (a) R_c and (b) R_h derived from A-Train, MERRA-2 and ERA-Interim from September 2006 - December 2010

Figure 3.4 summarizes the zonal mean of R_c and R_h. R_c in both reanalyses is generally more consistent than R_h, but there are obvious differences between A-Train and the reanalyses. For R_c, A-Train has a stronger cooling efficiency in the mid-latitudes from 30° N and 60° N, associated with the storm track region. The difference in the equatorial regional is caused by the underestimate of R_c over warm pool region by reanalyses discussed in Figure 3.3, but may also be related to precipitation biases. Over tropical areas, the bias between A-Train observations and reanalysis in R_h can also be clearly shown. The peak value of R_h in ERA-Interim, compared with

A-Train and MERRA-2, is more equatorial, which could result from a relatively narrower Hadley Circulation simulated by ERA-Interim than other reanalysis datasets (Nguyen et al. 2012). Overall, comparing the CIPs and EWCPs of A-Train, ERA-Interim and MERRA-2 show some significant differences, not only in the radiative parameters themselves, but how they are coupled to precipitation.

3.2 Environmental Regime Dependence

Both cloud regimes (Bony et al. 2004) and precipitation, and correspondingly, the strength of latent heating have a strong relationship to the environment (Huaman and Schumacher 2017). Here, we analyze the relationship between CIPs and several environmental variables including both thermodynamic (SST and CWV), and dynamic (vertical pressure velocity at 500hpa (ω_{500}), which is a proxy for the large-scale overturning circulation) variables. The analysis is focused on the EWCPs since the relationship between the radiation-only CIPs and the environment compare favorably between the observations and reanalyses (see Appendix).

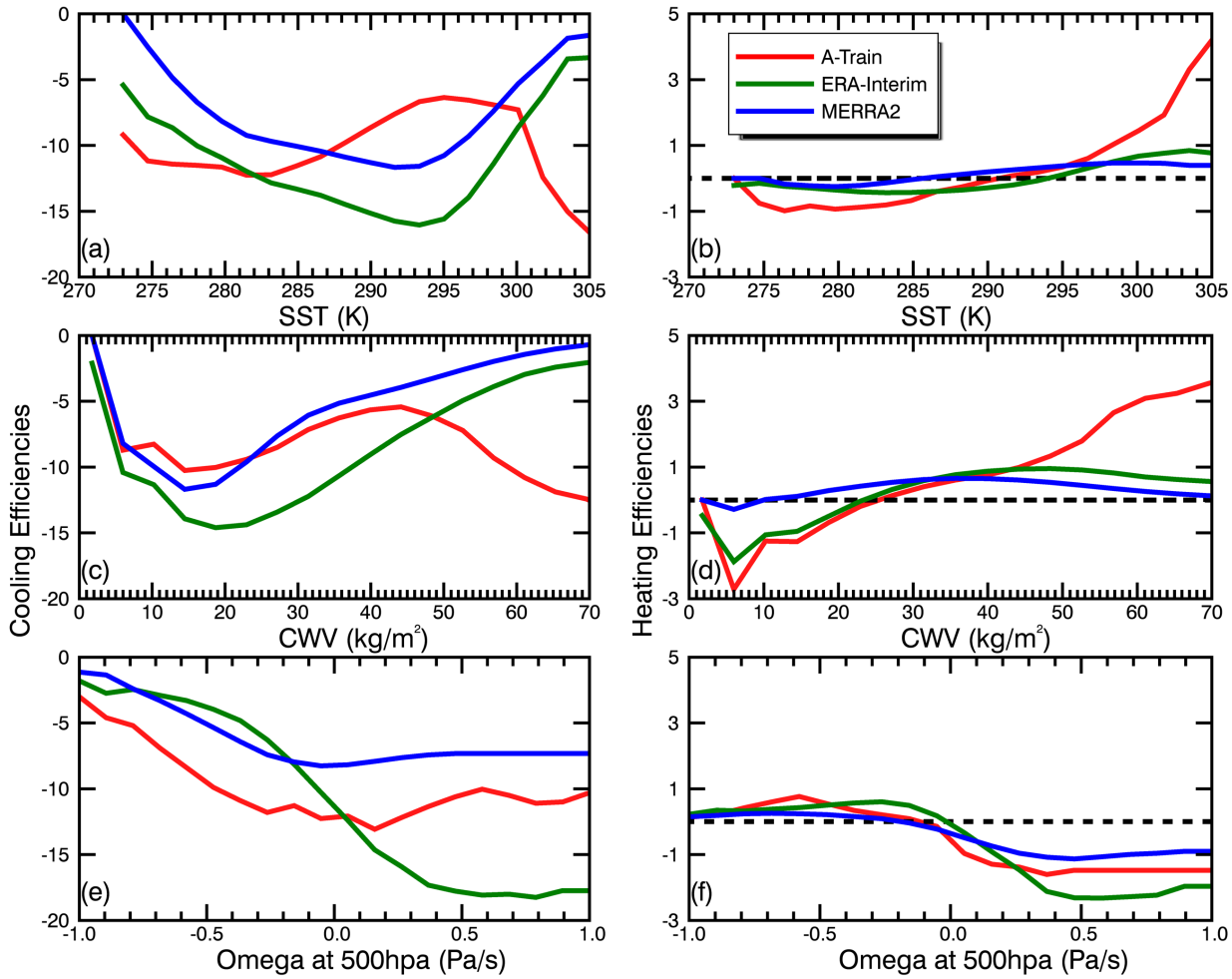

Figure 3.5: (a,c,e) R_c and (b,d,f) R_h as a function of (a,b) SST, (c,d) CWV, and (e,f) ω_{500}.

The relationships between R_c and R_h and the environmental variables are shown in Figure 3.5. In the left panels of Figure 3.5, A-Train results show that R_c is relatively strong at low SSTs and then weakens (represented by an increase) with increasing SST until about 295-300K. After this R_c rapidly decreases with increasing SST representing a strong cooling efficiency enhancement. In the results of both reanalyses, the trends at moderate and high SSTs are completely opposite. At low SSTs they both show strengthening R_c, however R_c continues to become strong until SSTs reach around 295 K, at which point they rapidly weaken. One of the reasons for the lack of strong

R_c in the reanalyses at high SSTs is that, as previously discussed, over the Indo-Pacific warm pool region, where SST is typically over 300 K, both of the reanalysis results fail to simulate the strong R_c that is shown in the A-Train results. This suggests that the reanalyses do not accurately couple the storm-scale precipitation and cloud radiative effects at high SSTs, either producing too much precipitation or too weak shortwave CRF. Another difference is in the position of the first minimum, which occurs at similar SST for both reanalyses but occurs at a much lower SST for A-Train. This discrepancy results from the differences in the extent of the regions demonstrating relatively large R_c in A-Train and reanalysis. The position of the first minimum is determined by strong R_c over the marine stratocumulus region and mid-latitudes. Strong R_c over marine stratocumulus regions in the A-Train results is confined to the Southern Ocean and regions along the coast where SSTs remain relatively low. In the rest of subtropics and in the southern hemisphere extratropics, A-Train reports a lower R_c. The global distributions in Figure 3.3 shows that regions of large R_c in reanalyses expand farther from the coasts toward the center of the ocean basins where SSTs are much warmer. However, reanalyses tend to produce lower cloud albedo and more precipitation over warmer SST regions. The differences combine to make R_c lower into regions of warmer SSTs.

By contrast, the patterns of R_h associated with SST in the three datasets don't vary as much with R_h increasing with increasing SST. Reanalysis results have a relatively lower range although they switch from low clouds that cool the atmosphere to clouds that heat the atmosphere at different SSTs with A-Train falling in between the two reanalyses. In general, the reanalyses show less cooling of the atmosphere at low SSTs and less heating of the atmosphere at high SSTs. The large differences between A-Train and the reanalyses simulating R_h at high SSTs is consistent with the

differences shown over the warm pool area in Figure 3.3 and suggests that the reanalyses underestimate the strength of the coupling in deep convective cloud systems typical of this region.

In Figure 3.5c-d, the relationship between CWV and the EWCPs for the three datasets is shown. The patterns are similar to SST in all the three datasets, where R_c of A-Train has two minima but both reanalysis results only have one. It is not surprising that the results indicate the change in EWCPs with CWV is highly associated with SST, but it is unknown which is the main driver. Many studies (Zhang et al. 1996; Bony et al. 2015; Trenberth et al. 2010) have shown a strong relationship between cloud radiative effects and SST, but studies also show a strong relationship between CWV and precipitation/latent heating (Bretherton et al. 2004; Peters and Neelin 2006; Neelin et al. 2009; Holloway and Neelin 2009; Ahmed and Schumacher 2015, 2016). However, from previous studies (Bony et al. 2004; Jakob et al. 2003; Jakob et al. 2005; Stephen 2005; Voigt and Shaw 2015), we know that both SST and CWV can contribute to the CRF and precipitation via different mechanisms, so a joint distribution of R_c and R_h with both variables will be examined in Figure 3.6 and 3.7 to determine which one is dominant in controlling R_c and R_h.

The link between EWCPs and dynamical regime is shown in Figure 3.5e-f. Figure 3.5e shows that R_c decreases as ω_{500} increases from negative (ascending regimes) to positive (subsidence regimes). Convective cloud regimes are generally associated with strong upward motion and typically accompanied by large precipitation and latent heat release, corresponding to a weaker R_c (assuming that the cloud forcing on the surface does not change). Positive ω_{500} is generally associated with a more stable atmosphere and the formation of low stratiform clouds where precipitation is usually small, but the cloud forcing on the surface could be very large leading to increased R_c. Both the observations and the reanalyses behave similarly, although they are closer in ascending regimes than in subsidence regimes where A-Train falls in between the two reanalysis

estimates. From the results of R_h, upward motion and downward motion obviously control the sign of R_h. For ascent regimes, R_h is positive and cloud heat the atmosphere more efficiently due to the enhancement of cloud greenhouse effect associated with deep convective clouds. For subsidence regimes, R_h is negative because the boundary layer tends to be more stable in these regimes and supports the formation of stratocumulus clouds, which will cool the atmosphere efficiently and produce little precipitation. Like R_c, the range of R_h estimates from A-Train and reanalyses appear to be closer in ascent regimes than in the subsidence regimes.

Given the strong covariability in SST, CWV, and dynamic regimes, it is not surprising that R_c and R_h appear to be influenced by more than one environment variable. In an attempt to determine which is the controlling variable, Figures 3.6 and 3.7 show the joint distributions of mean EWCPs conditionally sampled by combinations of different environmental variables. The first two rows of Fig. 3.6 show that the strength of R_c is largely controlled by the dynamic environment and that the observations and reanalyses are generally consistent. Clouds have strong cooling efficiencies in subsidence regimes and weaker ones in ascent regimes. Within the ascent regime the observations show enhanced cooling with thermodynamic regime changes, while the reanalysis shows a steady weakening which appears to be more controlled by CWV than SST especially in MERRA-2. In the subsidence regimes, A-Train shows a steady weakening of R_c beginning at moderate SST and CWV, which is not shown in the reanalyses. This is likely due to the expansion of the regions of large R_c away from the coast and toward regions of greater SST and CWV shown by the reanalyses in Figure 3.3. The relationship between R_c and the thermodynamic environment echoes the considerable differences between A-Train observations and reanalyses shown in Figure 3.5. The reanalyses appear to be somewhat more horizontally stratified, which indicates that CWV is a stronger control on R_c than SST in the reanalyses compared to the observations. In the observations,

below about 290K it is difficult to discern which thermodynamic variable is controlling R_c. For SST above 290K, holding SST fixed shows increasing R_c with CWV, but holding CWV fixed with increasing SST shows little variation, suggesting that above 290K CWV appears to control the strength of R_c. These results also indicate that the observations show much more distinction between the controls in different cloud regimes, while the reanalyses vary much more smoothly from one regime to another.

For R_h in Figure 3.7, it shows that clouds have strong positive heating efficiencies in ascent regions like the Indo-Pacific warm pool region and strong negative heating efficiencies in subsidence regimes, such as those dominated marine stratocumulus. The sign of R_h is largely controlled by the dynamic environment, which is also consistently shown in both A-Train observations and reanalyses. Clouds have strong negative heating efficiencies in subsidence regimes and strong positive heating efficiencies in ascent regimes. Within the ascent regime, A-Train results show an obvious trend in enhanced heating associated with the thermodynamic regime changes while the reanalysis show only a moderate enhanced heating, which is weakest in MERRA-2. This is likely due to the failure of reanalyses to simulate high R_h over warm pool regions as shown in Figure 3.3. From the last row, we can see that both the results of R_c and R_h indicate that CWV is a stronger control on both R_c and R_h than SST in the reanalyses compared to the observations. For R_h, even when SST increases beyond 300K, if there is not sufficient CWV, R_h shows little strengthening. But when CWV is sufficient, the strength of R_h rapidly increases. It demonstrates that clouds will heat the atmosphere more efficiently per unit rain, especially in deep convective cloud regimes, with both high SST and CWV. Also, when CWV increases, longwave emission to the surface decreases and the cloud greenhouse effect increases with the increase of cloud thickness and cloud top. The strength of the large-scale circulation has a strong control on

the magnitude of R_c, but with the strongest cooling at the tails of the SST/CWV domains. The sign of R_h is controlled by the large-scale circulation, while CWV appears to dominate in controlling the strength of R_h rather than SST.

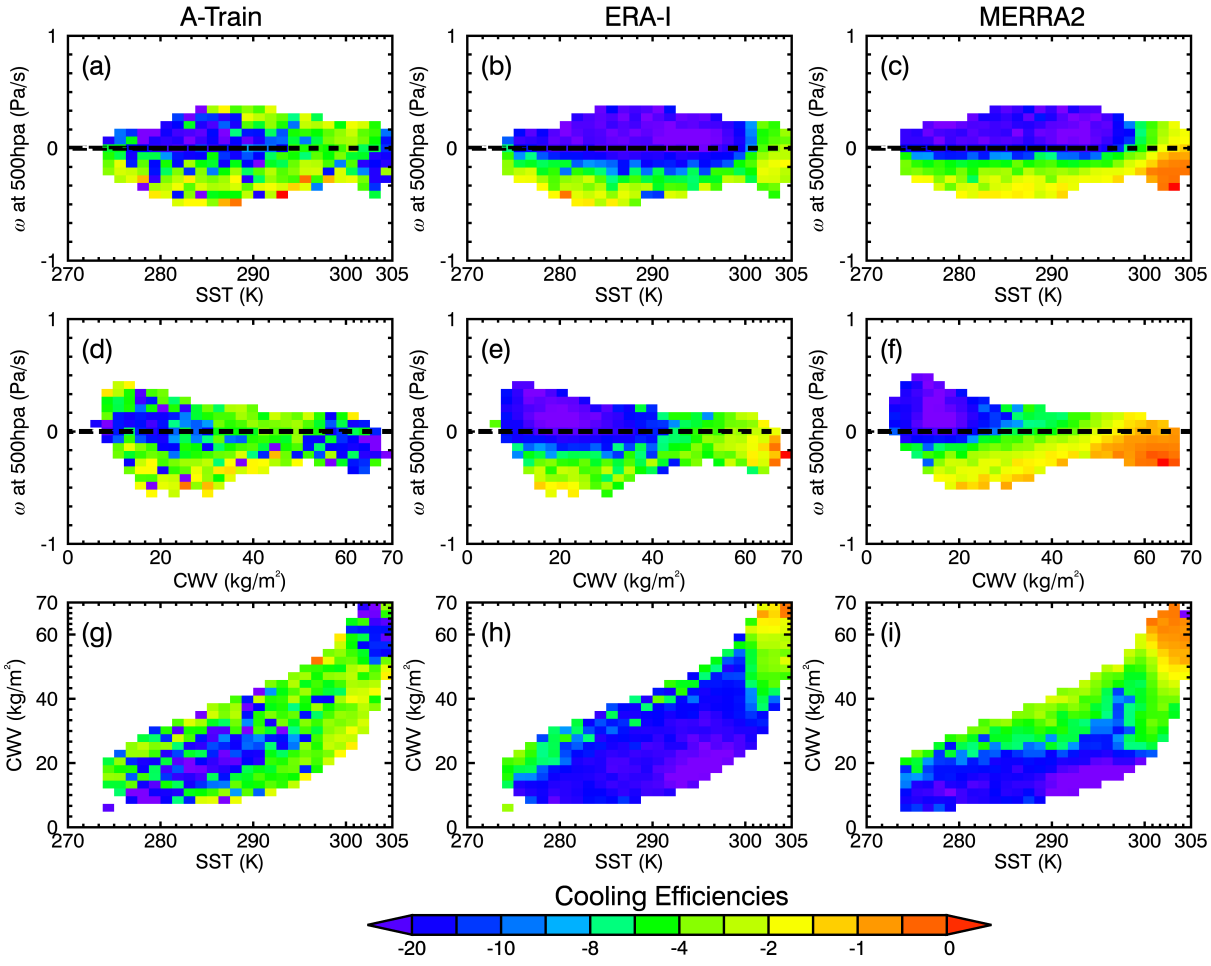

Figure 3.6: Joint distributions of mean R_c derived from A-Train/ERA-Interim/MERRA-2 as a function of (a-c) SST vs. ω_{500}, (d-f) CWV vs. ω_{500}, (g-i) SST vs. CWV from ERA-Interim

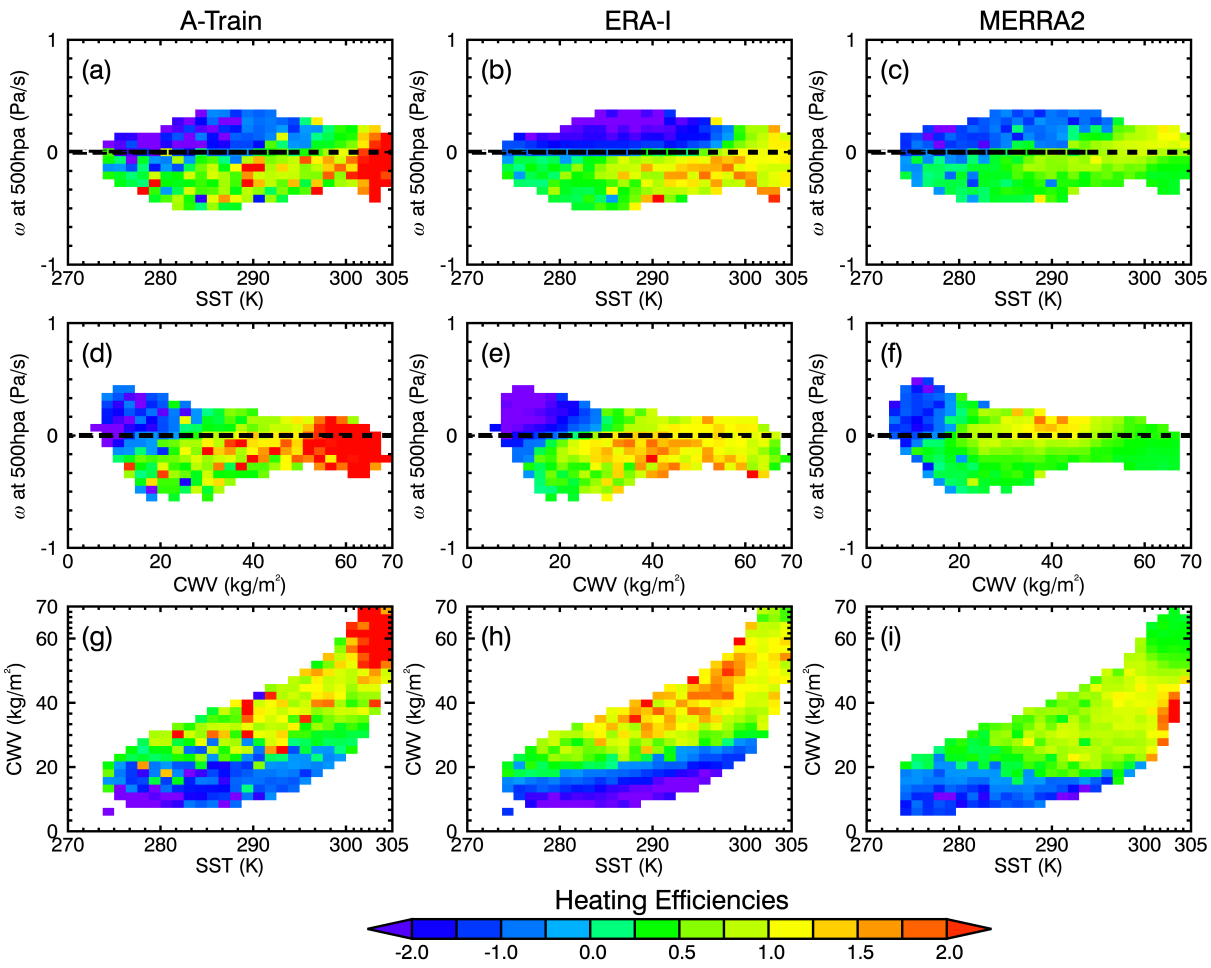

Figure 3.7: The same as Figure 3.6, but for R_h.

4. SUMMARY AND DISCUSSION

4.1 Conclusion

In this paper, we use A-Train observations and reanalyses to study three CIPs, G_c, A_c, N_c and two EWCPs, R_c and R_h, that connect the CRF and precipitation to present the cloud feedback properties of the climate system. R_c and R_h can also be connected to complex cloud feedback processes such as convective aggregation and the impact of shallow low clouds on the surface. Compared with the previous monthly averaged studies, we use a shorter time scale that is closer to the cloud and precipitation time scales to study the CIPs and EWCPs. The results are generally consistent with previous studies, however the range of values for the EWCPs is larger. CIPs are generally consistent in A-Train, ERA-Interim and MERRA-2. We use A-Train observations and reanalyses to focus on two EWCPs, R_c and R_h, that connect the CRF and precipitation. Not surprisingly, R_c and R_h are shown to vary with different cloud regimes. In regions dominated by stratocumulus, clouds tend to cool the surface and atmosphere more efficiently per unit latent heat release because stratocumulus regions have low rain rates and highly reflective clouds that results in large cloud SW radiative forcing. In this situation, both strong SW CRF and low rain rate contribute to strengthen R_c. For regions associated with deep convective clouds in environments with strong ascent and sufficient CWV, observations show that clouds cool the surface and heat the atmosphere more efficiently per unit latent heat release. Elevated and highly reflective cloud tops enhance both the cloud greenhouse effect and the cloud SW radiative cooling at surface.

We also evaluated EWCPs in ERA-Interim and MERRA-2 and find that they generally have similar global patterns as the observations. As models are always faced with the challenge of

simulating different cloud regimes, we found some possible limitations of reanalysis data in coupling cloud radiative effects and precipitation over DC regions. Both ERA-Interim and MERRA-2 show weaker R_c and R_h over the warm pool area where deep convective clouds prevail. The lower R_h values result from an underestimate of the LW CRF at TOA over tropical regions and/or an overestimate of precipitation. Moreover, when the EWCPs are composited for shorter time scales, there are larger biases in reanalysis EWCPs compared with observations than was shown for calculations at longer timescales (Daloz et al. 2018), so we suspect that the reanalysis is challenged more in capturing the coupling between the radiation and precipitation for shorter timescale variability like MJO.

For EWCPs, the dynamic regime appears to act as a switch with weak to strong surface cooling efficiencies and from atmospheric cooling to heating as the regime shifts from ascent to subsidence. The thermodynamic regime acts more as a control on the strength of the coupling parameters, especially for R_h. In ascent regimes, precipitating clouds go from weak to strong R_h with increasing SST and CWV, which suggests that clouds heat the atmosphere more efficiently per unit rainfall in warm and moist environments. Joint distributions of R_h as a function of SST and CWV in the observations indicate that CWV is the primary control, with relatively constant R_h across a range of SSTs for fixed CWV. Reanalyses capture the general relationships between EWCPs and their environment, with several important distinctions. Neither ERA-Interim nor MERRA-2 capture the strong cooling efficiencies at high SST and CWV, instead they have strong R_c from low to moderate SST and CWV which rapidly weaken at high SST and CWV suggesting that the coupling between precipitation and shortwave cloud forcing in these regimes is too weak in the reanalyses. Likewise, reanalyses also fail to capture the strong heating per unit precipitation with increasing

SST and CWV. They also do not appear to be as strongly linked with the environmental moisture as the observations.

Observational data inevitably have some uncertainties caused by the retrieval algorithms. For instance, 2BFLX partly overcomes the uncertainties of the radiative effects caused by low clouds, cirrus and aerosols, but there are still uncertainties in the SW fluxes, caused by the bias of LWC estimates and LW fluxes due to prescribed skin temperatures and the lower-tropospheric water vapor (Henderson et al. 2013). These uncertainties should be considered when comparing observational results and model outputs.

Even though over most of the globe, R_h and R_c are not large, Daloz et al. (2018) highlight the importance of R_h and R_c in these regions. For example, in failing to simulate R_c and R_h over the Indo-Pacific warm pool, reanalyses also do not capture a strong enough east-west gradient of R_c and R_h over the Pacific as in the A-Train results. However, as the transition of the precipitation gradient over Pacific becomes more pronounced during an ENSO event, the model response to the circulation becomes more sensitive to the latent heating variation (Schumacher et al. 2004). Also, a slight change over the West Pacific Ocean could have significant influence on the propagation of Madden-Julian Oscillation (MJO) that may not be captured in reanalysis or models. Daloz et al (2018) mentioned that R_h can be a good proxy for processes like convective aggregation. More aggregated convection will make the surrounding atmosphere drier and clearer and increase outgoing longwave radiation to the space (Bretherton et al. 2005; Tobin et al. 2012; Bony et al. 2015; Daloz et al 2018). In our observational results, R_h is high over the warm pool area and generally increases in regions of high CWV and SST, which indicates that the atmospheric radiative heating by deep convection increases faster than the precipitation power law scaling with CWV that has been shown in a number of studies (Masunaga and Bony 2018). This could imply

that cloud systems vary in such a way, perhaps via convective aggregation in moist regions, as to become more efficient at heating the atmosphere per unit rainfall to maintain global energy balance with the expanding dry regions.

Another inherent shortcoming of reanalyses such as MERRA-2 and ERA-Interim is that cloud properties are still exclusively modelled due to difficulties in assimilating cloud-affected satellite radiances or properly assimilating the cloud properties themselves. The parameterizations in numerical weather prediction (NWP) are similar, if not identical, to the ones used in GCMs. Even though reasonable parameterizations have been developed, it remains challenging to balance the system regarding simplicity, realism, computational stability and efficiency in NWP, reanalysis, and GCMs.

4.2 Future Work

Based on the current studies, we suspect that CIPs and EWCPs also depend on the cloud microphysical properties, like liquid water content, cloud droplet concentration, cloud optical depth etc. and the specific details of cloud types like stratocumulus, stratus, altocumulus, altostratus and cirrus, etc. In the future, the EWCPs can be compared with those in GCMs or cloud resolving models to understand how well models couple precipitation and radiation, what parameterizations need to be improved to better capture the coupling, and more about the underlying physical processes driving the observed relationship between EWCPs and their environment. This survey of cloud impacts will also be complemented by an analysis of cloud radiative kernels generated from satellite observations to provide observational constraints on effective climate sensitivity in the present-day climate system. In addition, the differences between

our results and the monthly-averaged results of Daloz et al (2018) show that the values of CIPs and EWCPs are both temporally and spatially dependent and they should be set accordingly in climate models. We have tested multiple averaging methods, from individual pixel-level to gridded calculations for the satellite observation data, to ultimately use in comparisons between observations and climate models. Averaging the observations at different spatial resolutions simulates the climate model gridded outputs, so that we can test how the spatial resolution of climate models affect the sensitivity of the relationship between CRF and precipitation. The CIPs and EWCPs presented here provide an effective way to link both cloud radiative properties and precipitation properties together to demonstrate the synergistic effects of the cloud-precipitation-radiation interaction (CPRI).

REFERENCES

Ahmed, F., and C. Schumacher, 2015: Convective and stratiform components of the precipitation-moisture relationship. Geophys. Res. Lett., 42, 10 453–10 462, doi:10.1002/2015GL066957.

Ahmed, F., C. Schumacher, Z. Feng, and S. Hagos, 2016: A retrieval of tropical latent heating using the 3D structure of precipitation features. J. Appl. Meteor. Climatol., 55, 1965– 1982, https://doi.org/10.1175/JAMC-D-15-0038.1.

Allan, R. P., 2009: Examination of relationships between clear-sky longwave radiation and aspects of the atmospheric hydrological cycle in climate models, reanalyses, and observations. J. Climate, 22, 3127–3145.

Allan, R. P., 2011: Combining satellite data and models to estimate cloud radiative effect at the surface and in the atmosphere. Meteor. Appl., 18, 324–333.

Andrew, T., P.M.Forster, O. Boucher, N. Bellouin, and A. Jones, 2010: Precipitation, radiative forcing and global temperature change. Geophys. Res. Lett., 37, L14701.

Behrangi, A., M. Lebsock, S. Wong, and B. Lambrigtsen, 2012: On the quantification of oceanic rainfall using spaceborne sensors. J. Geophys. Res., 117, D20105.

Behrangi, Y. Tian, B. H. Lambrigtsen, and G. L. Stephens, 2014b: What does CloudSat reveal about global land precipitation detection by other spaceborne sensors? Water Resour. Res., 50, 4893–4905.

Betts A. K., R. Desjardins, D. Worth, and B. Beckage, 2014: Climate coupling between temperature, humidity, precipitation, and cloud cover over the Canadian Prairies. J. Geophys. Res. Atmos., 119, 13 305–13 326.

Bodas-Salcedo, A., M. J. Webb, M. E. Brooks, M. A. Ringer, K. D. Williams, S. F. Milton, and D. R.Wilson, 2008: Evaluating cloud systems in the Met Office global forecast model using simulated CloudSat radar reflectivities. J. Geophys. Res.,113, D00A13.

Bony S, Dufresne JL, Le Treui H, Morcrette JJ, Snior C (2004) On dynamic and thermodynamic components of cloud changes. Clim Dyn 22:71–86.

Bony S, and Coauthors, 2015: Clouds, circulation and climate sensitivity. Nat. Geosci., 8, 261–268.

Bony S, and J. Dufresne, 2005: Marine boundary layer clouds at the heart of tropical cloud feedback uncertainties in climate models. Geophys. Res. Lett., 32, L20806.

Bosilovich, M. G., and Coauthors, 2015b: MERRA-2: Initial evaluation of the climate. NASA/TM-2015-104606, Vol. 43, 139 pp.

Bosilovich, M. G., R. Lucchesi, and M. Suarez, 2016: MERRA-2: File specification. GMAO Office Note 9, 73 pp.

Bosilovich, M. G., F. Robertson, L. Takacs, A. Molod, and D. Mocko, 2017: Atmospheric water balance and variability in the MERRA-2 reanalysis. J. Climate, 30, 1177–1196.

Bouniol, D., R. Roca, T. Fiolleau, and E. Poan, 2016: Macrophysical, microphysical, and radiative properties of tropical mesoscale convective systems along their life cycle. J. Climate, 29, 3353–3371.

Bretherton, C.S. and A.H. Sobel, 2002: A Simple Model of a Convectively Coupled Walker Circulation Using the Weak Temperature Gradient Approximation. J. Climate, 15,2907–2920.

Bretherton, C.S., C. S., M. E. Peters, and L. E. Back, 2004: Relationships between water vapor path and precipitation over the tropical oceans. J. Climate, 17, 1517–1528.

Bretherton, C.S., P. N. Blossey, and M. Khairoutdinov, 2005: An energy-balance analysis of deep convective self-aggregation above uniform SST. J. Atmos. Sci., 62, 4273–4292.

Calisto, M., D. Folini, M. Wild, and L. Bengtsson, 2014: Cloud radiative forcing intercomparison between fully coupled CMIP5 models and CERES satellite data. Ann. Geophys., 32, 793–807.

Ceppi, P., F. Brient, M. D. Zelinka, and D. L. Hartmann, 2017: Cloud feedback mechanisms and their representation in global climate models. Wiley Interdiscip. Rev.: Climate Change, 8, e465.

Choi, Y.-S., C.-H. Ho, C.-E. Park, T. Storelvmo, and I. Tan, 2014: Influence of cloud phase composition on climate feedbacks. J. Geophys. Res. Atmos., 119, 3687–3700.

Clark A.J., W.A.Gallus Jr., and T.-C. Chen (2007) Comparison of the Diurnal Precipitation Cycle in Convection-Resolving and Non-Convection-Resolving Mesoscale Models. Mon. Wea. Rev., 135, 3456–3473.

Colman, R. A., 2015: Climate radiative feedbacks and adjustments at the Earth's surface. J. Geophys. Res. Atmos., 120, 3173– 3182.

Cullather, R. I., S. M. J. Nowicki, B. Zhao, and M. J. Suarez, 2014: Evaluation of the surface representation of the Greenland ice sheet in a general circulation model. J. Climate, 27, 4835–4856.

Dai, A., and K. E. Trenberth, 2004: The diurnal cycle and its depiction in the Community Climate System Model. J. Climate, 17, 930–951.

Dai, F., R. Yu, X. Zhang, Y. Yu, and J. Li, 2003: The impact of low-level cloud over the eastern subtropical Pacific on the "double ITCZ" in LASG FGCM-0. Adv. Atmos. Sci., 20, 461–474.

Daloz, A., E. Nelson, T. L'Ecuyer, A. Rapp, and L. Sun, 2018: Assessing the coupled influences of clouds on the Atmospheric Energy and Water Cycles in Reanalyses with A-Train Observations. J. Climate.

Dee D. P., Uppala S. M., Simmons A. J., Berrisford P., Poli P., Kobayashi S., Andrae U., Balmaseda M. A., Balsamo G., Bauer P., Bechtold P., Beljaars A. C. M., van de Berg L., Bidlot J., Bormann N., Delsol C., Dragani R., Fuentes M., Geer A. J., Haimberger L., Healy S. B., Hersbach H., Hólm E. V., Isaksen L., Kållberg P., Köhler M., Matricardi M., McNally A. P., Monge-Sanz B. M., Morcrette J.-J., Park B.-K., Peubey C., de Rosnay P., Tavolato C., Thépaut J.-N. and Vitart, F. (2011) The ERA-Interim reanalysis: configuration and performance of the data assimilation system. Q.J.R. Meteorol. Soc., 137: 553–597.

Dessler, A. E., 2010: A determination of the cloud feedback from climate variations over the past decade. Science, 330, 1523–1527.

Dinh, T. and S. Fueglistaler, 2017: Mechanism of fast atmospheric energetic equilibration following radiative forcing by CO_2 J. Adv. Model. Earth Syst. 9 2468–2482.

Dolinar E.K., Dong X. and Xi B. (2016): Evaluation and Intercomparison of clouds, precipitation and radiation budgets in recent reanalyses using satellite-surface observations. Clim. Dyn. 46:2123-2144.

Duynkerke, P. G., and J. Teixeira, 2001: Comparison of the ECMWF reanalysis with FIRE I observations: Diurnal variation ofmarine stratocumulus. J. Climate, 14, 1466–1478, https://doi.org/10.1175/1520-0442(2001)014,1466:COTERW.2.0.CO;2.

Eitzen, Z., K. Xu, and T. Wong, 2011: An estimate of low-cloud feedbacks from variations of cloud radiative and physical properties with sea surface temperature on interannual time scales. J. Climate, 24, 1106–1121.

Gelaro, R., W. McCarty, M.J. Suárez, R. Todling, A. Molod, L. Takacs, C.A. Randles, A. Darmenov, M.G. Bosilovich, R. Reichle, K. Wargan, L. Coy, R. Cullather, C. Draper, S. Akella, V. Buchard, A. Conaty, A.M. da Silva, W. Gu, G. Kim, R. Koster, R. Lucchesi, D. Merkova, J.E. Nielsen, G. Partyka, S. Pawson, W. Putman, M. Rienecker, S.D. Schubert, M. Sienkiewicz, and B. Zhao, 2017: The Modern-Era Retrospective Analysis for Research and Applications, Version 2 (MERRA-2). J. Climate, 30, 5419–5454.

Gibson, J. K., and Coauthors, 1997: ERA description. ECMWF Re-Analysis Project Report Series, 72 pp.

Global Hydrology Resource Center/MSFC/NASA (2009), AMSR-E L2 Rainfall Subset, collocated with CloudSat track V002, Edited by GES DISC, Greenbelt, MD, USA, Goddard Earth Sciences Data and Information Services Center (GES DISC), Accesse: 09-01-2017, https://disc.gsfc.nasa.gov/datacollection/AMSRERR_CPR_002.html

Grabowski, W. W., Bechtold, P., Cheng, A., Forbes, R., Halliwell, C., Khairoutdinov, M., Lang, S., Nasuno, T., Petch, J., Tao, W.-K., Wong, R., Wu, X. and Xu, K.-M. (2006), Daytime convective development over land: A model intercomparison based on LBA observations. Q.J.R. Meteorol. Soc., 132: 317–344.

Griggs, J., and J. Bamber, 2008: Assessment of cloud cover characteristics in satellite datasets and reanalysis products for Greenland. *J. Climate*, **21**, 1837–1849.

Haynes, J. M., and G. L. Stephens (2007), Tropical oceanic cloudiness and the incidence of precipitation: Early results from CloudSat, Geophys. Res. Lett., 34, L09811.

Haynes, J. M., T. S. L'Ecuyer, G. L. Stephens, S. D. Miller, C. Mitrescu, N. B. Wood, and S. Tanelli, 2009: Rainfall retrieval over the ocean with spaceborne W-band radar. J. Geophys. Res., 114, D00A22.

Held, I. M., and B. J. Soden, 2006: Robust responses of the hydrological cycle to global warming. J. Climate, 19, 5686–5699.

Henderson, D.S., T. L'Ecuyer, G. Stephens, P. Partain, and M. Sekiguchi, 2013: A Multisensor Perspective on the Radiative Impacts of Clouds and Aerosols. J. Appl. Meteor. Climatol., 52, 853–871.

Holloway, C. E., and J. D. Neelin, 2009: Moisture vertical structure, column water vapor, and tropical deep convection. J. Atmos. Sci., 66, 1665–1683, doi:10.1175/2008JAS2806.1.

Huaman, L., C. Schumacher, 2017: Assessing the vertical latent heating structure of the East Pacific ITCZ using the CloudSat CPR and TRMM CPR. J. Climate, 31, 2563-2577.

Itterly, K. F., and P. C. Taylor, 2014: Evaluation of the tropical TOA flux diurnal cycle in MERRA and ERA-Interim retrospective analyses. J. Climate, 27, 4781–4796.

Jakob, C. and Klein, S. A. (2000), A parametrization of the effects of cloud and precipitation overlap for use in general-circulation models. Q.J.R. Meteorol. Soc., 126: 2525–2544.

Jakob, C., and G. Tselioudis, 2003: Objective identification of cloud regimes in the tropical western Pacific. Geophys. Res. Lett., 30, 2082.

Jakob, C., and G. Tselioudis, and T. Hume, 2005: The radiative, cloud, and thermodynamic properties of the major tropical western Pacific cloud regimes. J. Climate, 18, 1203–1215.

Kay, J., and Coauthors, 2012: Exposing global cloud biases in the Community Atmosphere Model (CAM) using satellite observations and their corresponding instrument simulators. J. Climate, 25, 5190–5207.

Kim, D., M.-S. Ahn, I.-S. Kang, and A. D. Del Genio, 2015: Role of longwave cloud–radiation feedback in the simulation of the Madden–Julian oscillation. J. Climate, 28, 6979–6994.

Kim, J. and M.J. Alexander, 2013: Tropical Precipitation Variability and Convectively Coupled Equatorial Waves on Sub-monthly Time Scales in Reanalyses and TRMM. J. Climate, 26, 3013–3030.

Klein, S. A., and D. L. Hartmann, 1993: The seasonal cycle of low stratiform clouds. *J. Climate*, **6**, 1587–1606.

Kiehl, J.T., 1994: On the Observed Near Cancellation between Longwave and Shortwave Cloud Forcing in Tropical Regions. J. Climate, 7, 559–565,https://doi.org/10.1175/1520-0442(1994)007<0559:OTONCB>2.0.CO;2

Kohler M., Ahlgrimm M., Beljaars A.C.M. (2011) Unified treatment of dry convective and stratocumulus-topped boundary layers in the ECMWF model. Q.J.R. Meteo. Sci. 137:43-57.

Kubar, T. L., D. E. Waliser, J. L. Li, and X. Jiang, 2012: On the annual cycle, variability, and correlations of oceanic lowtopped clouds with large-scale circulation using Aqua MODIS and ERA-Interim. J. Climate, 25, 6152–6174.

Kummerow, C. D., S. Ringerud, J. Crook, D. Randel, and W. Berg, 2011: An observationally generated a priori database for microwave rainfall retrievals. J. Atmos. Oceanic Technol., 28, 113–130.

Kummerow, C. D., D. L. Randel, M. Kulie, N-Y. Wang, R. Ferraro, S. J. Munchak, and V. Petkovic, 2015: The evolution of the Goddard profiling algorithm to a fully parametric scheme. J. Atmos. Oceanic Technol.

Larson, K., and D. L. Hartmann and S. A. Klein, 1999: The role of clouds, water vapor, circulation, and boundary layer structure in the sensitivity of the tropical climate. J. Climate, 12, 2359–2374.

Larson, K., and D. L. Hartmann, 2003a: Interactions among cloud, water vapor, radiation, and large-scale circulation in the tropical climate. Part I: Sensitivity to uniform sea surface temperature changes. J. Climate, 16, 1425–1440.

Larson, K., and D. L. Hartmann, 2003b: Interactions among cloud, water vapor, radiation, and large-scale circulation in the tropical climate. Part II: Sensitivity to spatial gradients of sea surface temperature. J. Climate, 16, 1441–1455.

Lee, M.-I, I.-S. Kang, J.-K. Kim, and B. E. Mapes, 2001: Influence of cloud-radiation interaction on simulating tropical intraseasonal oscillation with an atmospheric general circulation model. J. Geophys. Res. 106, 14219-14233.

Lebsock, M. D., and T. S. L'Ecuyer, 2011: The retrieval of warm rain from CloudSat. J. Geophys. Res., 116, D20209.

Lebsock, M. D., T. S. L'Ecuyer, D. Vane, G. Stephens, and D. Reinke, 2011: Level 2C RAIN-PROFILE product process description and interface control document, algorithm version 0.0. JPL Rep., 14 pp., http://www.cloudsat.cira.colostate.edu/sites/default/files/products/files/2C-RAIN-PROFILE-PDICD.P_R04.20110620.pdf.

Level 2B Fluxes and Heating Rates and 2B Fluxes and Heating Rates w/ Lidar Process Description and Interface Control Document, CloudSat Team, 2006.

L'Ecuyer, T. S., H. Masunaga, and C. Kummerow, 2006: Variability in the characteristics of precipitation systems in the tropical Pacific. Part II: Implications for atmospheric heating. J. Climate, 19, 1388–1406.

L'Ecuyer, T. S. and G. L. Stephens, 2007: The Tropical Atmospheric Energy Budget from the TRMM Perspective. Part II: Evaluating GCM Representations of the Sensitivity of Regional Energy and Water Cycles to the 1998-99 ENSO Cycle, J. Climate 20, 4548-4571.

L'Ecuyer, T. S., N.B. Wood, T. Haladay, G.L. Stephens, and P.W. Stackhouse Jr., 2008: Impact of clouds on atmospheric heating based on the R04 CloudSat fluxes and heating rates dataset. J. Geophys. Res., 113, D00A15.

Li, J. L., X. H. Zhang, Y. Q. Yu, and F. S. Dai, 2004: Primary reasoning behind the double ITCZ phenomenon in a coupled ocean-atmosphere general circulation model. Adv. Atmos. Sci., 21, 857–867.

Liu, Y. and J. R. Key, 2016: Assessment of Arctic cloud cover anomalies in atmospheric reanalysis products using satellite data. *J. Climate*, **29**, 6065–6083.

Liu, Y. and Q. Zhang, 2014: The CloudSat radar–lidar geometrical profile product (RL-GeoProf): Updates, improvements, and selected results. J. Geophys. Res. Atmos., 119, 9441–9462.

Mace, G. G., and S. Benson, 2017: Diagnosing cloud microphysical process information from remote sensing measurements—A feasibility study using aircraft data. Part I: Tropical anvils measured during TC4. J. Appl. Meteor. Climatol., 56, 633–649.

Mace, G. G., Q. Zhang, M. Vaughan, R. Marchand, G. Stephens, C. Trepte, and D. Winker, 2009: A description of hydrometeor layer occurrence statistics derived from the first year of merged CloudSat and CALIPSO data. J. Geophys. Res., 114, D00A26, doi:10.1029/2007JD009755.

Masunaga, H., and T. S. L'Ecuyer, 2011: Equatorial asymmetry of the east Pacific ITCZ: Observational constraints on the underlying processes. J. Climate, 24, 1784–1800, doi:https://doi.org/10.1175/2010JCLI3854.1.

Mlawer E.J., Taubman S.J., Brown P.D., Iacono M.J., Clough S.A. (1997) Radiative transfer for inhomogeneous atmospheres: RRTM, a validated correlated-k model for the longwave. J. Geophys. Res. 102D:16663-16682.

Molod A., L. Takacs, M.Suarez and J. Bacmeister, 2015: Development of the GEOS-5 general circulation model: evolution from MERRA to MERRA2. Geosc. Model. Ev., 8, 1339-1356.

Moorthi, S., and M. J. Suarez, 1992: Relaxed Arakawa–Schubert: A parameterization of moist convection for general circulation models. Mon. Wea. Rev., 120, 978–1002, doi:https://doi.org/10.1175/1520-0493(1992)120<0978:RASAPO>2.0.CO;2.

Muller, C. J., and I. M. Held, 2012: Detailed investigation of the self-aggregation of convection in cloud-resolving simulations. J. Atmos. Sci., 69, 2551–2565, https://doi.org/10.1175/JAS-D-11-0257.1.

Muller, C. J. and S. Bony, 2015: What favors convective aggregation and why? Geophys. Res. Lett., 42, 5626–5634, doi:10.1002/2015GL064260.

Naud, C. M., J. F. Booth, and A. D. Del Genio, 2014: Evaluation of ERA-Interim and MERRA cloudiness in the Southern Ocean. J. Climate, 27, 2109–2124, https://doi.org/10.1175/JCLI-D-13-00432.1.

Neelin, J. D., O. Peters, and K. Hales, 2009: The transition to strong convection. J. Atmos. Sci., 66, 2367–2384, doi:10.1175/ 2009JAS2962.1.

Nguyen, H., A. Evans, C. Lucas, I. Smith, and B. Timbal, 2013: The Hadley circulation in reanalyses: Climatology, variability, and change. J. Climate, 26, 3357–3376, https://doi.org/10.1175/ JCLI-D-12-00224.1.

O'Gorman, P. A., R. P. Allan, M. P. Byrne, and M. Previdi, 2012: Energetic constraints on precipitation under climate change. Surv. Geophys., 33, 585–608, doi:10.1007/ s10712-011-9159-6.

O'Brien, T. A., F. Li, W. D. Collins, S. A. Rauscher, T. D. Ringler, M. A. Taylor, S. M. Hagos, and L. R. Leung, 2013: Observed scaling in clouds and precipitation and scale incognizance in regional to global atmospheric models. J. Climate, 26, 9313– 9333, doi:10.1175/JCLI-D-13-00005.1.

Pendergrass, A. G., and D. L. Hartmann, 2014: The atmospheric energy constraint on global-mean precipitation change. J. Climate, 27, 757–768, doi:https://doi.org/10.1175/JCLI-D-13-00163.1.

Peters, O., and J. D. Neelin, 2006: Critical phenomena in atmospheric precipitation. Nat. Phys., 2, 393–396.

Previdi, M., 2010: Radiative feedbacks on global precipitation. Environ. Res. Lett., 5, 025211, doi:10.1088/1748-9326/5/2/025211.

Rädel, G., T. Mauritsen, B. Stevens, D. Dommenget, D. Matei, K. Bellomo, and A. Clement, 2016: Amplification of El Niño by cloud longwave coupling to atmospheric circulation. Nat. Geosci., 9, 106–110, https://doi.org/10.1038/ngeo2630.

Randall, D. and Coauthors, 2007: Climate models and their evaluation. Climate Change 2007: The Physical Science Basis. Contribution of Working Group I to the Fourth Assessment Report of the Intergovernmental Panel on Climate Change, S. Solomon, D. Qin, M. Manning, Z. Chen, M. Marquis, K. Averyt, M. Tignor, and H. Miller, Eds., Cambridge University Press, Cambridge, 589-662.

Ritter, B., and J.-F. Geleyn, 1992: A comprehensive radiation scheme for numerical weather prediction models with potential applications in climate simulations. *Mon. Wea. Rev.*, **120**, 303–325.

Schumacher, C., R. A. Houze Jr., and I. Kraucunas, 2004: The tropical dynamical response to latent heating estimates derived from the TRMM precipitation radar. J. Atmos. Sci., 61, 1341–1358.

Sobel and H. Gildor, 2003: A simple time-dependent model of SST hot spots. J. Climate, 16, 3978–3992.

Song, X., and G. Zhang, 2009: Convection parameterization, tropical Pacific double ITCZ, and upper-ocean biases in the NCAR CCSM3. Part I: Climatology and atmospheric feedback. J. Climate, 22, 4299–4315.

Stengel, M., Schlundt, C., Stapelberg, S., Sus, O., Eliasson, S., Willén, U., and Meirink, J. F.: Comparing ERA-Interim clouds with satellite observations using a simplified satellite simulator, Atmos. Chem. Phys. Discuss, in review, 2018

Stephens, G. L., and T. J. Greenwald, 1991: The Earth's radiation budget in relation to atmospheric hydrology: 2. Observations of cloud effects. J. Geophys. Res., 96, 15 325–15 340, https://doi.org/10.1029/91JD00972.

Stephens, G., 2005: Cloud feedbacks in the climate system: A critical review. J. Climate, 18, 237–273.

Stephens, G. and Coauthors, 2008: CloudSat mission: Performance and early science after the first year of operation. J. Geophys. Res., 113, D00A18.

Stephens, G. and T. D. Ellis, 2008: Controls of global-mean precipitation increases in global warming GCM experiments. J. Climate, 21, 6141-6155.

Stephens, G. and Coauthors, 2010: Dreary state of precipitation in global models. J. Geophys. Res., 115, D24211.

Stephens, G. D. Winker, J. Pelon, C. Trepte, D. Vane, C. Yuhas, T. L'Ecuyer, and M. Lebsock, 2017: CloudSat and CALIPSO within the A-Train: Ten years of actively observing the Earth system. Bull. Amer. Meteor. Soc., 0.

Sassen, K., Z. Wang, and D. Liu, 2008: The global distribution of cirrus clouds from CloudSat/Cloud–Aerosol Lidar and Infrared Pathfinder Satellite Observations (CALIPSO) measurements. J. Geophys. Res., 113, D00A12.

Stevens, B., and S. Bony, 2013: What are climate models missing? Science, 340, 1053–1054.

Kociuba, G., and S. B. Power, 2015: Inability of CMIP5 models to simulate recent strengthening of the Walker circulation: Implications for projections. J. Climate, 28, 20–35.

Tanelli, S., S. L. Durden, E. Im, K. S. Pak, D. G. Reinke, P. Partain, J. M. Haynes, and R. T. Marchand, 2008: CloudSat's Cloud Profiling Radar after two years in orbit: Performance, calibration, and processing. IEEE Trans. Geosci. Remote Sens., 46, 3560–3573.

Tobin, I., S. Bony, and R. Roca, 2012: Observational evidence for relationships between the degree of aggregation of deep convection, water vapor, surface fluxes, and radiation. J. Climate, 25, 6885–6904.

Trenberth, K. E., J. T. Fasullo, C. O'Dell, and T. Wong, 2010: Relationships between tropical sea surface temperature and top-of-atmosphere radiation. Geophys. Res. Lett., 37, L03702.

Turk, F. J., and S. D. Miller, 2005: Toward improved characterization of remotely sensed precipitation regimes with MODIS/ AMSR-E blended data techniques. IEEE Trans. Geosci. Remote Sens., 43, 1059–1069.

Uppala, S. M., and Coauthors, 2005: The ERA-40 re-analysis. Quart. J. Roy. Meteor. Soc., 131, 2961–3012, https://doi.org/10.1256/qj.04.176.

Voigt, A., and T. A. Shaw, 2015: Circulation response to warming shaped by radiative changes of clouds and water vapour. Nat. Geosci., 8, 102–106.

Waliser, D. E., R. Murtugudde, and L. Lucas, 2003: Indo-Pacific Ocean response to atmospheric intraseasonal variability. Part I: Austral summer and the Madden-Julian Oscillation. J. Geophys. Res., 108.3160.

Wang, S., and A. H. Sobel, 2011: Response of convection to relative sea surface temperature: Cloud-resolving simulations in two and three dimensions. J. Geophys. Res., 116, D11119.

Wilcox, E. M., and V. Ramanathan, 2001: Scale dependence of the thermodynamic forcing of tropical monsoon clouds: Results from TRMM observations. J. Climate, 14, 1511–1524.

Wilheit, T., C. Kummerow, and R. Ferraro, 2003: Rainfall algorithms for AMSR-E. IEEE Trans. Geosci. Remote Sens., 41, 204–214.

Wood, R., 2012: Stratocumulus clouds. Mon. Wea. Rev., 140, 2373-2423.

Xu, K.-M., T. Wong, B. A. Wielicki, L. Parker, and Z. A. Eitzen, 2005: Statistical analyses of satellite cloud object data from CERES. Part I: Methodology and preliminary results of 1998 El Niño/2000 La Niña. J. Climate, 18, 2497–2514.

Xu, K.-M., A. Cheng, and M. Zhang, 2010: Cloud-resolving simulation of low-cloud feedback to an increase in sea surface temperature. J. Atmos. Sci., 67, 730–748.

Xu, K.-M., T. Wong, S. Dong, F. Chen, S. Kato, and P. C. Taylor, 2016a: Cloud object analysis of CERES Aqua observations of tropical and subtropical cloud regimes, Part I: Four-year climatology. J. Climate, 29, 1617–1638.

Ying, J., and P. Huang, 2016: Cloud–radiation feedback as a leading source of uncertainty in the tropical Pacific SST warming pattern in CMIP5 models. J. Climate, 29, 3867–3881, doi:10.1175/JCLI-D-15-0796.1.

Zhang, M. H., R. D. Cess, and S. C. Xie, 1996: Relationship between cloud radiative forcing and sea surface temperatures over the entire tropical oceans. J. Climate, 9, 1374–1384.

APPENDIX

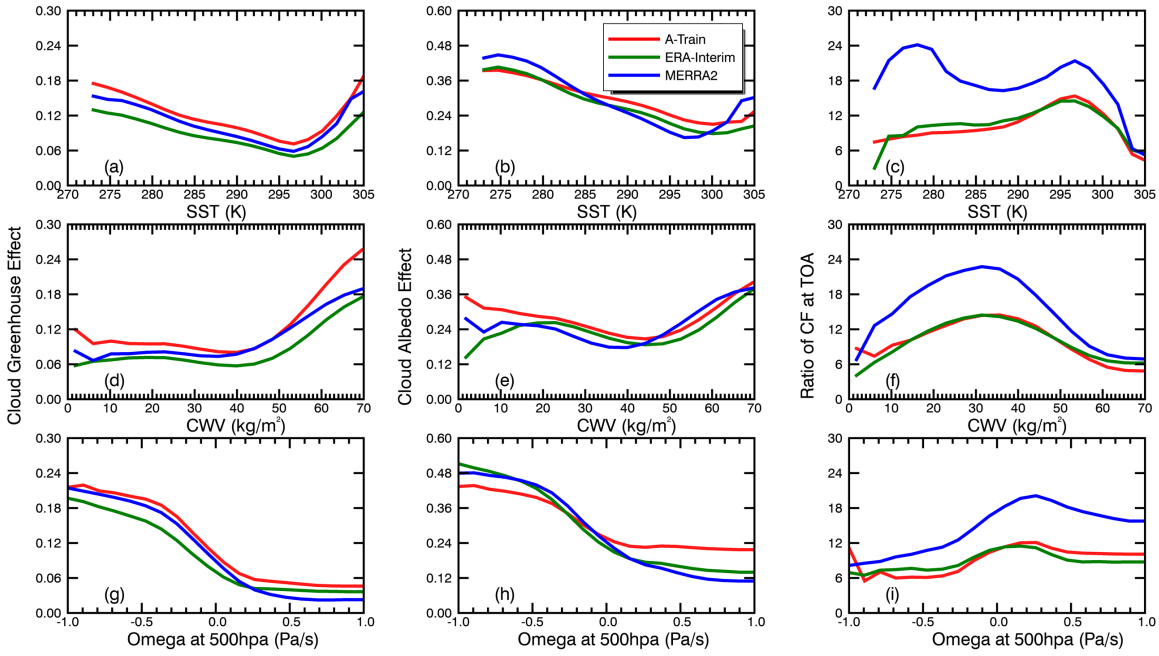

Figure A.1: (a,d,g) G_c , (b,d,h) A_c and (c,f,i) N_c as a function of (a-c) SST, (d-f) CWV, and (g-i) ω_{500}.

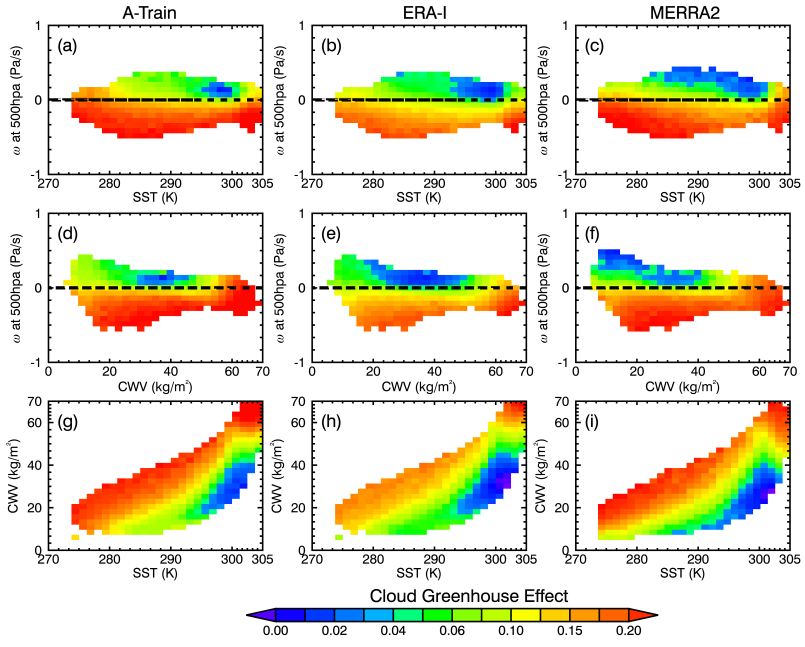

Figure A.2: The same as Figure A.1, but for G_c.

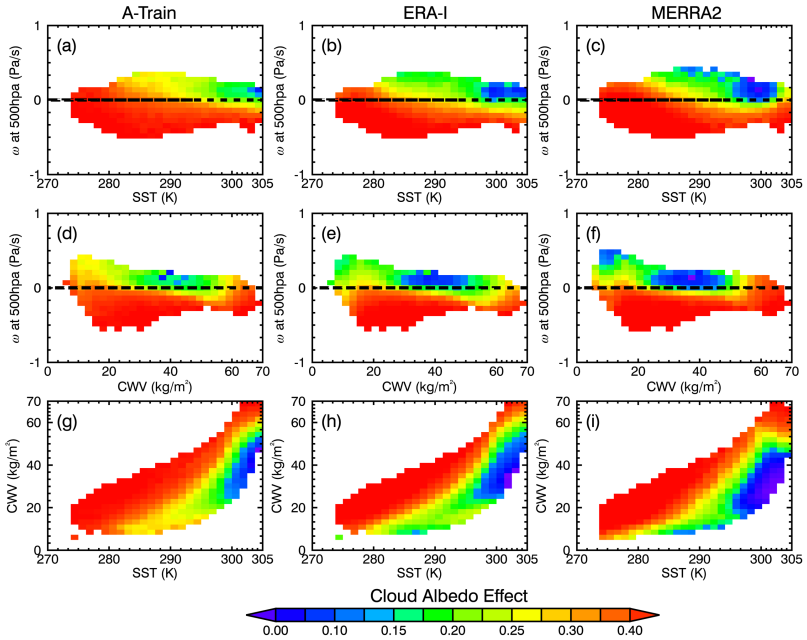

Figure A.3: The same as Figure A.1 but for A_c.

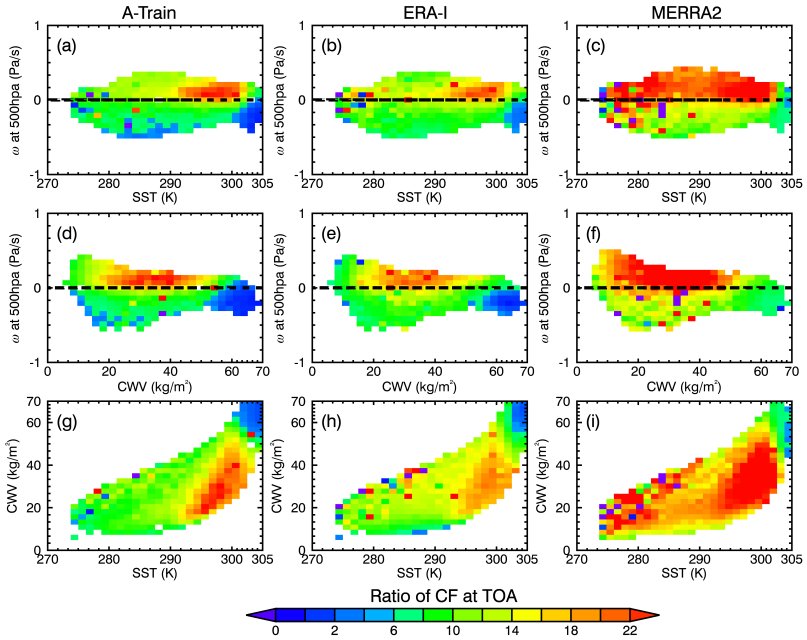

Figure A.4: The same as Figure A.1 but for N_c.